Chapter in **Advancing Astrophysics with the SKA – II**

Solar Radio Bursts in the metric to kilometric range

Anshu Kumari[1], Mugundhan V.[2], Diana E. Morosan[3,4], Jasmina Magdalenić[5,6], Ketaki Deshpande[5,6], Peijin Zhang[7,8], Divya Paliwal[1,9], Pietro Zucca[10] and Puja Majee[11]

[1] *Udaipur Solar Observatory, Physical Research Laboratory, Dewali, Badi Road, Udaipur - 313001, Rajasthan, India*

[2] *Dept. of Space Planetary Astronomical Sciences and Engineering (SPASE), IITK, Kanpur 208016, India*

[3] *Department of Physics and Astronomy, University of Turku, 20014, Turku, Finland*

[4] *Turku Collegium for Science, Medicine and Technology, University of Turku, 20014, Turku, Finland*

[5] *Center for mathematical Plasma Astrophysics (CmPA), KU Leuven, Celestijnenlaan 200B, 3001 Leuven, Belgium*

[6] *Solar-Terrestrial Centre of Excellence (STCE), Royal Observatory of Belgium, Avenue Circulaire 3, 1180 Uccle, Belgium*

[7] *Center for Solar-Terrestrial Research, New Jersey Institute of Technology, Newark, NJ 07102, USA*

[8] *Cooperative Programs for the Advancement of Earth System Science, University Corporation for Atmospheric Research, Boulder, CO, USA*

[9] *Indian Institute of Technology, Gandhinagar, Gujarat-382355, India*

[10] *ASTRON, The Netherlands Institute for Radio Astronomy, Oude Hoogeveensedijk 4, 7991 PD Dwingeloo, The Netherlands*

[11] *National Centre for Radio Astrophysics, Tata Institute of Fundamental Research, S. P. Pune University Campus, Pune 411007, India*

E-mail: anshu@prl.res.in

Solar radio bursts (SRBs) are intense emissions observed in radio wavelengths most frequently during solar transients, such as coronal mass ejections (CMEs) and flares. SRBs are direct signatures of accelerated electrons in the solar atmosphere. These solar transients have a direct impact on the near-Earth atmosphere. SRBs serve as key diagnostic tools for plasma processes, particle accelerations, magnetic field dynamics in the solar corona and the heliosphere, which are the root cause of these solar transients. There are several key science question which solar radio observations can answer, such as: When & where is the bulk of the energy released in flares?, what are the physical properties of the energy release site?, what are the properties of heated plasma & accelerated particles?, how does the transport of heated plasma & accelerated particles?, what bearing do flares have on the question of coronal heating? The Square Kilometre Array (SKA), with its unprecedented sensitivity, temporal, spectral, and spatial resolution, as well as dynamic range, is expected to provide an enhanced understanding of the physics behind solar transients with unprecedented detail.

© The Authors

1 Introduction

Solar radio emission was historically divided into three main components: emission originating from the quiet Sun, emission associated with bright active regions, and radio emission associated with solar eruptive phenomena. Herein, we focus on the metric and decametric solar radio bursts (< 500 MHz), which is generally of a significantly higher intensity than the quiet Sun emission. Solar radio bursts are associated with either the emission of active regions or eruptive phenomena, such as solar flares and coronal mass ejections (CMEs). Radio bursts are generally classified based on the spectral appearance of the bursts, and the wavelength regimes of their appearance (Wild, 1950; Suzuki and Dulk, 1985; Nelson and Melrose, 1985b; McLean and Labrum, 1985), which is closely related to the emission mechanisms of the radio bursts (Newkirk, 1961a; Melrose, 1980; Dulk, 1985). Considering the morphological characteristics, five main categories of solar radio bursts can be distinguished: Type I, Type II, Type III, Type IV, and Type V. A detailed description is provided in Section 3.1.

Solar radio bursts are observed across a wide range of wavelengths, from millimetres to kilometres, corresponding to frequencies from the GHz to the kHz range. Observations at short wavelengths correspond to distances close to the solar surface, while those at long wavelengths correspond to the large distances from the Sun. This means that radio bursts map the processes occurring at nearly all levels of the solar corona, extending as far away from the Sun as interplanetary space. Such a broad coverage makes solar radio bursts a powerful diagnostic tool for mapping the coronal plasma properties (see e.g. Vršnak et al., 2001, 2002; Vršnak et al., 2003; Kumari, 2019; Deshpande et al., 2025), or tracking the propagation of their exciters (see e.g. Magdalenić et al., 2008; Magdalenić et al., 2014; Kumari et al., 2017a; Zhang et al., 2019; Kumari et al., 2017b,c; Jebaraj et al., 2020; Morosan et al., 2022a; Zucca et al., 2025). At microwave frequencies, solar radio bursts are typically dominated by gyrosynchrotron emission from mildly relativistic electrons in flaring loops. These phenomena provide complementary diagnostics of magnetic fields and energetic particles but are not treated in detail here.

The Square Kilometre Array (SKA) will transform solar and heliospheric radio science by offering unprecedented sensitivity, dynamic range, broadband spectral coverage with high spectral, temporal, and spatial resolution, high fidelity, and wideband imaging spectropolarimetry across decimetric–metric-centimetre (Nindos et al., 2019). With its capability for high-cadence, wideband imaging spectropolarimetry, SKA will enable systematic estimation of coronal magnetic fields, plasma turbulence, particle acceleration, and shock dynamics using radio bursts, with a level of precision previously unattainable. This information is highly important, not only for our better understanding of the physics of solar phenomena, but also for being employed as boundary conditions and validation means for different models addressing processes at both kinetic and magnetohydrodynamic (MHD) scales.

In this review, we introduce the general phenomenology of solar radio bursts, summarise the state of current radio observations from ground- and space-based instruments, and highlight the limitations imposed by sensitivity, dynamic range, and sparse sampling of the corona. We then discuss in detail how SKA, through its widespread baseline distribution, accurate polarization calibration, and extremely dense instantaneous u–v coverage, will overcome many of these challenges. Particular

emphasis is placed on SKA's potential to image radio bursts and their fine structures, quantify coronal magnetic topology via gyroresonance and gyrosynchrotron diagnostics and polarization observations of plasma emission, trace shock evolution and SEP source regions with unprecedented accuracy, and enable synergistic science with solar missions such as Solar Orbiter (SolO; Müller et al., 2020), Parker Solar Probe (PSP; Fox et al., 2016), Aditya-L1 (Tripathi et al., 2023) and PROBA3 (Zhukov et al., 2025). Together, these capabilities position SKA as the key facility for the next generation of solar and heliospheric radio science.

2 Solar Radio Observational Techniques

In observations of solar radio emission, we distinguish four different techniques, resulting in four distinct types of radio data: single-frequency measurements, dynamic spectra, radio imaging, and direction-finding observations.

2.1 Single Frequency Observations

From the beginning of the radio observations until about 1950, all radio observations were based on single-frequency measurements that recorded both the continuum emission and radio bursts in the received radiation flux. Single-frequency data are radio polarimeter recordings with a relative frequency bandwidth typically ranging around df/f = 0.2 per cent. The currently operational single–frequency solar radio observatories, together with their frequency ranges and typical observing times, are summarised in Figure 1.

Currently, single-frequency radio observations are not very frequent, for example, the Gauribidanur Radio SpectroPolarimeter (GRIP) (Ramesh et al., 2013) and the Radio Solar Telescope Network (RSTN) (Giersch and Kennewell, 2022). The RSTN is operated by the United States Air Force and consists of four ground-based solar radio observatories—Sagamore Hill, Palehua, Learmonth, and San Vito—collectively known as the Radio Solar Telescope Network (RSTN). Each site continuously monitors solar radio emission at eight fixed frequencies (245, 410, 610, 1415, 2695, 4995, 8800, and 15400 MHz). The Learmonth Solar Observatory (Kennewell and Cornelius, 1983) is jointly operated by the Bureau of Meteorology (Australia) and the USAF. The Ventspils International Radio Astronomy Center (VIRAC; Bezrukovs et al., 2012) RT-32 in Irbene, Latvia, performs single-dish test observations in the 6.3–9.3 GHz range, offering measurements in 16 frequency bands in both right circular polarization (RCP) and left circular polarization (LCP). At the Kislovodsk Mountain Astronomical Station of the Pulkovo Observatory (Russia), the RT-2 and RT-3 antennas operate at 6.15 and 9.35 GHz, with routine observations conducted between 05:00 and 13:00 UT. Real-time data have been available since April 2002, with archival observations dating back to 1957. The Siberian Solar Radio Telescope (SSRT; Smolkov et al., 1986) in Irkutsk provides correlation curves at 4.5, 5.2, 6.0, 6.8, and 7.5 GHz, while the Siberian Radioheliograph (SRH; Lesovoi et al., 2017), also located in Irkutsk, supplies correlation plots (Stokes I and V) at the same frequencies, with continuous observations commencing in July 2016. The Solar Submillimeter-wave Telescope (SST; Kaufmann et al., 2008) at El Leoncito, Argentina, measures full-Sun emission at 212 and 405 GHz using a cluster of six beams (four with HPBW $\sim 4'$ at 212 GHz and two with HPBW $\sim 2'$ at 405 GHz). The SSRT spectropolarimeter, operating between 2–24 GHz across 16 discrete

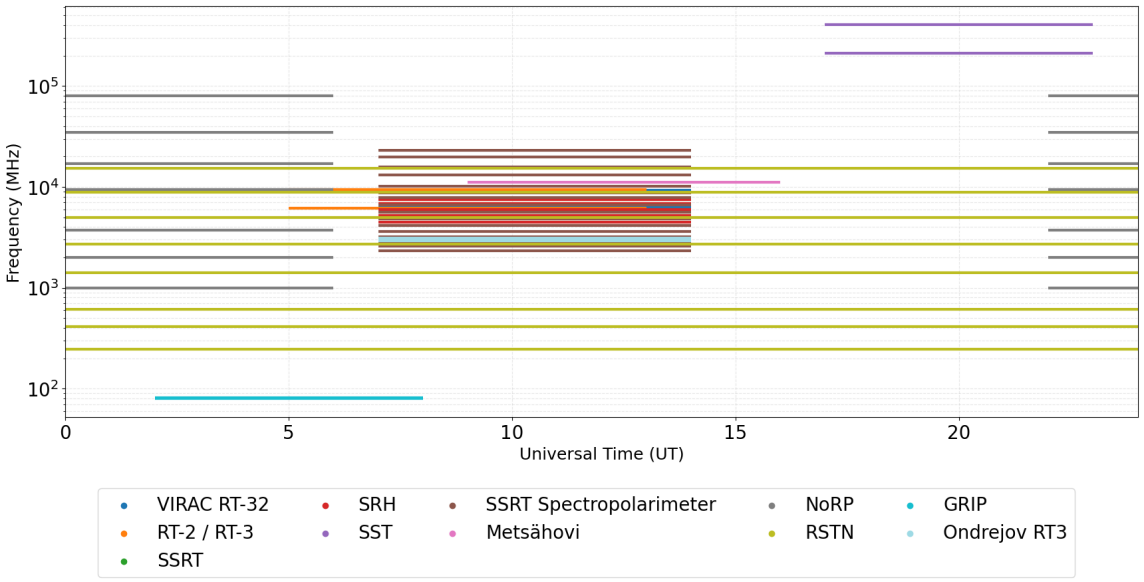

Figure 1: Daily observing windows and operational frequency ranges of non-imaging solar radio flux and light-curve instruments. Each horizontal bar represents the combined time–frequency coverage for a specific instrument, plotted in UT (horizontal axis) and frequency in MHz (vertical axis, logarithmic scale). These instruments measure integrated solar radio flux at one or multiple discrete frequencies, providing high-cadence time series used to study flare energetics, emission mechanisms, event timing, and long-term solar radio variability. Instruments with observing sessions crossing midnight (e.g., NoRP) are represented with two split rectangles. Together, these facilities offer continuous global monitoring across 1–400 GHz, which is crucial for characterizing impulsive and slowly varying solar radio emissions.

channels (2.34–22.93 GHz), provides daily dual-polarization (RCP/LCP) data since March 2011. The Metsähovi Radio Observatory (MRO) in Finland observes the Sun at 11.2 GHz with a 1 kHz sampling rate, recording data continuously from sunrise to sunset since 2001. The Ondřejov Solar Radio Observatory (Czech Republic) operates a single–frequency solar radio monitoring system at 3 GHz [1]. The Nobeyama Radio Polarimeters (NoRP) in Japan monitor full-disk solar emission at 1, 2, 3.75, 9.4, 17, 35, and 80 GHz with a time resolution of 0.1 s, providing one of the longest and most frequently used high-cadence datasets for solar activity studies (Nakajima et al., 1985).

The example of fluctuations of the solar radio emission at a single frequency is shown in Figure 2. Presented observations were taken by the solar multichannel radio polarimeter of the Trieste Solar Radio System (TSRS; Messerotti and Zlobec, 2001) of the INAF-Trieste Astronomical Observatory. Observations of the integrated full disk emission were taken at a high temporal resolution, i.e., a sampling rate of 1000 Hz (1 ms). The TSRS instrument also provided very important additional information on the polarization of the recorded radiation, i.e., measurements of the flux density in LCP and RCP. The radio energy measured at the Earth, i.e. flux density, is in solar flux units sfu, where 1 sfu=10^{-22} $W\ m^{-2}\ Hz^{-1}$. The TSRS instrument is unfortunately no longer operational. It should be noted that single-frequency observations are often strongly affected by the interference from local TV, radio emissions and other terrestrial radio sources.

[1] https://space.asu.cas.cz/~radio/

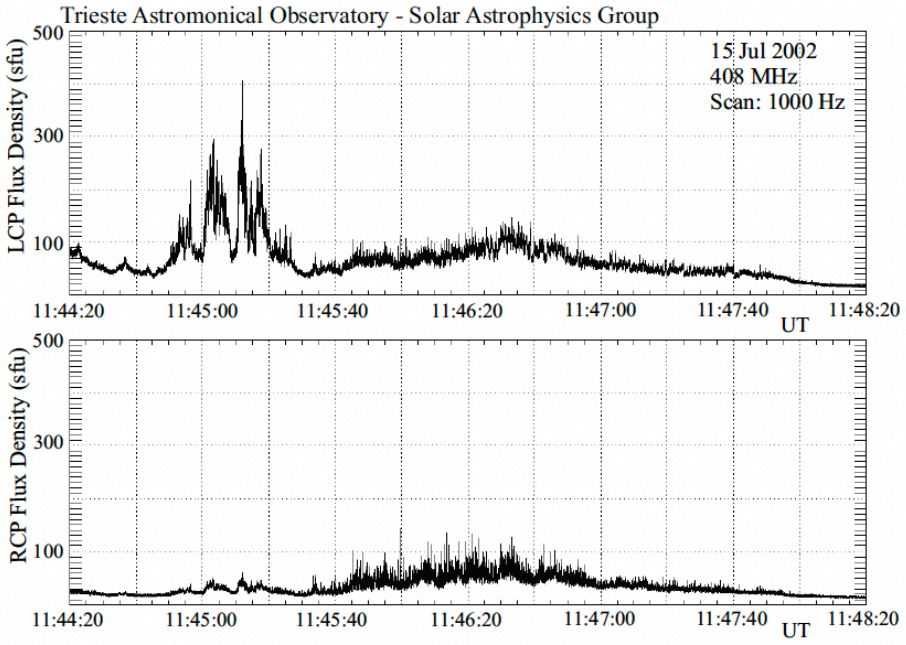

Figure 2: Single frequency data, i.e. time series of the flux density in sfu, recorded by the solar multi-channel radiopolarimeter of the TSRS. The flux density, i.e., the L-hand and R-hand circular polarization measurements (top and bottom panel, respectively), were routinely taken in the metric range. In the first 80s of recordings, the structured continuum is strongly L-polarized (about 90 %), and the continuum in the following 160s is weakly L-polarized. (Modified from Magdalenić (2008)).

One of the most frequently used single frequencies, which is also considered a proxy for solar activity, is the so-called 10.7cm flux observations. Continuous monitoring of the solar radio flux at microwave frequencies (typically near 2.8 GHz) is one of the most reliable long-term indicators of solar magnetic activity. The 10.7 cm (2.8 GHz) solar flux index, commonly referred to as the F10.7 flux, has been routinely measured since 1947 at the Dominion Radio Astrophysical Observatory (DRAO) in Canada, providing an uninterrupted record spanning over seven decades. This index is highly correlated with the evolution of active regions, sunspot numbers, and extreme ultraviolet (EUV) irradiance, making it an essential proxy for tracking solar cycle variability. Complementary measurements at neighbouring frequencies, such as the 2.7 GHz observations from the Learmonth Solar Observatory in Australia, extend and support global monitoring efforts, ensuring continuity in the event of local interruptions or adverse weather conditions. Because the F10.7 flux responds sensitively to changes in the solar chromosphere and low corona, it is widely used in operational space-weather models, thermospheric–ionospheric density predictions, and satellite drag calculations. Despite its apparent simplicity as a single-frequency radio measurement, the F10.7 index remains one of the most robust and extensively utilised empirical parameters in heliophysics, linking solar activity to geospace response. With the continuously increasing number of radio interference sources, F10.7 flux observations, even in the 'protected frequency band', are being significantly endangered and are becoming less frequent.

2.2 Dynamic Spectrometer and Spectropolarimeters

Using only single-frequency measurements often makes it difficult to distinguish between different types of radio bursts, and additionally, the information about the frequency span of the bursts is lacking. Wild and McCready (1950) introduced the technique of acquiring the dynamic spectra of radio bursts where the intensities are recorded continuously, as a function of frequency over a given frequency range. The radio spectrogram, also known as a dynamic radio spectrum, is a graphical representation of the radio emission intensity recorded at a number of closely spaced single frequencies as a function of time. The currently operational spectrometers and spectropolarimeters for solar radio observatories, together with their frequency ranges and typical observing times, are summarised in Figure 3. Dynamic spectra are often defined as frequency-time diagrams with colour-coded intensity of the radio emission. Following the convention, the observing frequency in the metric wavelength range is presented, decreasing from top to bottom in Figure 4. The dynamic spectra recorded at longer wavelengths by the space-based radio instrument are generally presented with the frequency decreasing from the bottom to the top, opposite to the metric range convention (Figure 4). Dynamic spectra can be formed in several different ways. The previously often employed receivers, which "sweep" through the frequencies, measure radio emission at one frequency for a short time interval and then at the next instant at the following higher/lower frequency. The metric range observations are often impacted by the radio frequency interferences (RFIs). Horizontal, uniformly coloured stripes (mostly white), often seen in dynamic spectra extending across the entire plot, are artificial emissions, i.e., interference from sources such as TV and radio stations.

Whole-sun dynamic spectra are provided by several dedicated broadband radio spectrographs operating worldwide. The URAN–2 system in Poltava, Ukraine, observes in the 8–33 MHz range with dual polarization, a time resolution of 1–100 ms, and a frequency resolution of 4 kHz, offering a dynamic range of about 90 dB. The Observatory for Solar Radio Astronomy (OSRA) at Tremsdorf (Germany) operated between 40–800 MHz from 1954 to 2007, providing one of the longest-running spectral datasets. The Siberian Solar Radio Telescope (SSRT) in Irkutsk (Russia) supplies spectral observations in the 4–8 GHz range with 26 frequency channels and dual circular polarization; 1-s cadence data are publicly available, while 10-ms resolution data can be requested for detailed studies. The Gauribidanur Low-Frequency Solar Spectrograph (GLOSS) in India routinely monitors the 35–85 MHz range (recently upgraded to 35–435 MHz) with a cadence of 0.25 s, providing daily spectra and an extensive archive of type II bursts since 2009[2]. The Gauribidanur RAdio Solar Spectropolarimeter (GRASP) in India routinely monitors the 50–500 MHz range with a cadence of 0.25 s, providing daily spectra in Stokes-I and Stokes-V (Kumari, 2015). High-resolution observations at decimetric and metric wavelengths are provided by the Humain Solar Radio Spectrograph (HSRS) in Belgium, operating between 275–1495 MHz with roughly 12,500 channels and a cadence of 0.25 s [3]. The Hiraiso Radio Spectrograph (HiRAS) in Japan spans an exceptionally wide band of 25–2500 MHz and has been delivering continuous solar dynamic spectra since 1996 [4]. The Learmonth Solar Radio Spectrograph (Australia) sweeps through 25–180 MHz every three seconds and remains an important component of long-term solar

[2] https://www.iiap.res.in/centers/gro/grids
[3] https://www.sidc.be/humain/home
[4] https://solarobs.nict.go.jp/radio.html

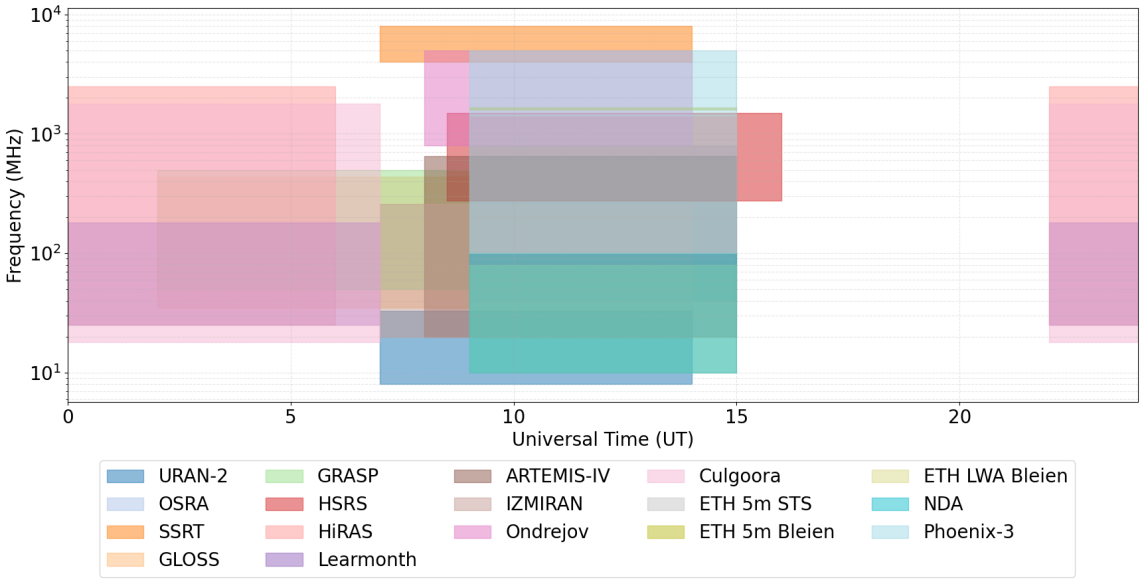

Figure 3: Operating time windows and frequency coverage for major solar dynamic spectrometers and spectropolarimeters that record full-Sun radio spectra with fine spectral and temporal resolution. These instruments produce dynamic spectra essential for identifying and classifying solar radio bursts (Types I–V), diagnosing electron acceleration, tracing the propagation of CMEs/shocks, and probing coronal/heliospheric plasma. Frequency ranges span from long-wavelength decametric systems (e.g., URAN-2 at 8–33 MHz) to microwave spectrometers (e.g., SSRT 4–8 GHz) and high-frequency broadband systems such as Phoenix-3 (100–5000 MHz). Many facilities operate only during local daytime (e.g., Humain, Trieste, Gauribidanur), while others maintain seasonal schedules (e.g., SSRT spectrograph). Instruments are shown excluding the distributed CALLISTO network, focusing instead on dedicated high-performance spectrometers with long-term archives. This global ensemble provides near-continuous spectral coverage from 10 MHz to several gigahertz, enabling comprehensive studies of solar radio bursts.

monitoring. Ondřejov Solar Radio Telescopes (Czech Republic) provide detailed dynamic spectra in the 2–4.5 GHz range, which are widely used for studying coherent microwave bursts. Additional low-frequency dynamic spectra have historically been supplied by the Green Bank Solar Radio Burst Spectrometer (GBSRBS; White et al., 2005) in the USA (see Figure 4), which operated from 18 to 70 MHz until 2012 (GBSRBS; White et al., 2005), and by the Culgoora Solar Radio Spectrograph (Australia), which surveyed 18 to 1800 MHz with a three-second sweep cadence for several decades. Complementary measurements at centimetric wavelengths are obtained using the ETH Zurich 5-m dish in Bleien, Switzerland, which observes between 1590 and 1650 MHz with a temporal resolution of 0.25 s. At lower frequencies, the ETH Zurich LWA system at Bleien covers 10–80 MHz with dual circular polarization, 0.25-s cadence, and a 300-kHz bandwidth. Finally, the Phoenix-3 spectrograph (Bleien, Switzerland) provides high-quality dynamic spectra from 100 to 5000 MHz at a sub-second cadence (≈0.1 s) with 5000 spectral channels, offering one of the most detailed broadband datasets currently available. The e-CALLISTO network is a globally distributed set of low-cost, programmable spectrometers designed for continuous monitoring of solar radio emission in the 45–870 MHz range. Built around the CALLISTO receiver concept developed at ETH Zurich (Benz et al., 2009), the network provides near-24-hour coverage of solar

radio bursts and RFI environments, with up to 400 channels per sweep and a typical time resolution of 0.25 seconds, making it a crucial resource for heliophysics research, education, and space weather monitoring [5].

The dynamic radio spectra are also affected by the radio emissions of terrestrial origin. However, due to the continuous and broadband mapping of radio emission along the range of frequencies, the effect is somewhat smaller than in the case of single-frequency observations.

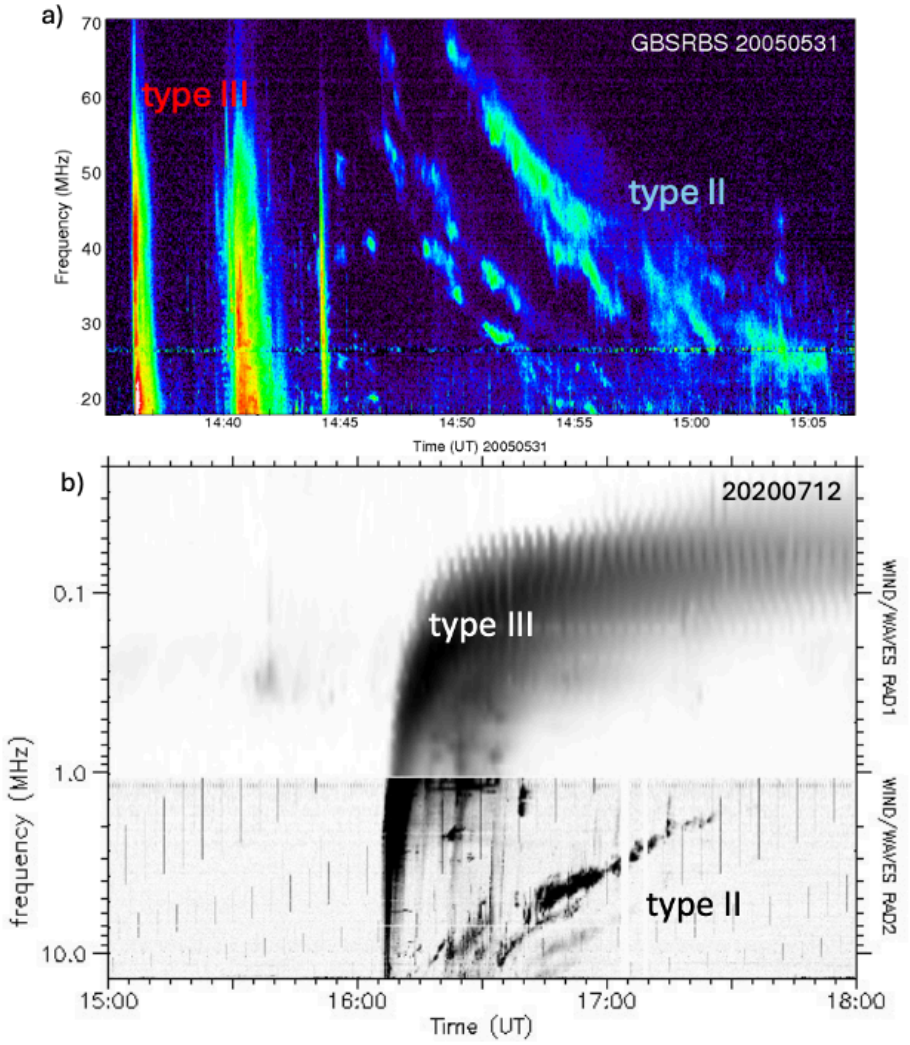

Figure 4: Dynamic spectra observed by ground-based and space-based instruments, panels a) and b) respectively. The slowly drifting type II radio bursts, i.e. signatures of shock waves and fast drifting type III radio bursts, i.e. signatures of fast electron beams, are marked in two spectra. a) Dynamic radio spectrum observed by Green Bank Solar Radio Burst Spectrometer in the frequency range 70–18 MHz, observed on May 31, 2005. b) The radio emission in DH to km wavelength range observed by WIND/Waves instrument (Bougeret et al., 1995) on December 7, 2020.

[5] https://www.e-callisto.org/Data/data.html

2.3 Solar Radio Imaging

Imaging observations of the solar corona at radio wavelengths are essential for locating emission sources, tracking coronal dynamics, and linking radio bursts to underlying plasma processes. One of the most important radio instruments, which has provided solar radio images for several decades and whose observations have resulted in numerous publications and several breakthroughs in solar radio physics, is the Nançay Radioheliograph (NRH; Kerdraon and Delouis, 1997). The NRH instrument is located in France and consists of two linear, cross-shaped antenna arrays: an East-West arm with 19 antennas distributed along a 3,200 m baseline, and a North-South arm with 24 antennas spanning 1,250 m. Together, these provide 576 interferometric visibilities. The instrument observes presently at ten fixed frequencies between 150 and 450 MHz (150.9, 228.0, 298.7, 382.2, 432.0, 173.2, 270.6, 327.0, 408.0, and 444.0 MHz), enabling true two-dimensional snapshot imaging of the solar corona at a cadence of up to 8 images per second. With its digital correlator and dense instantaneous *uv*-coverage, the NRH routinely delivers high-quality images of metric-wavelength emission, including all types of radio bursts and their substructures. NRH data are publicly available[6].

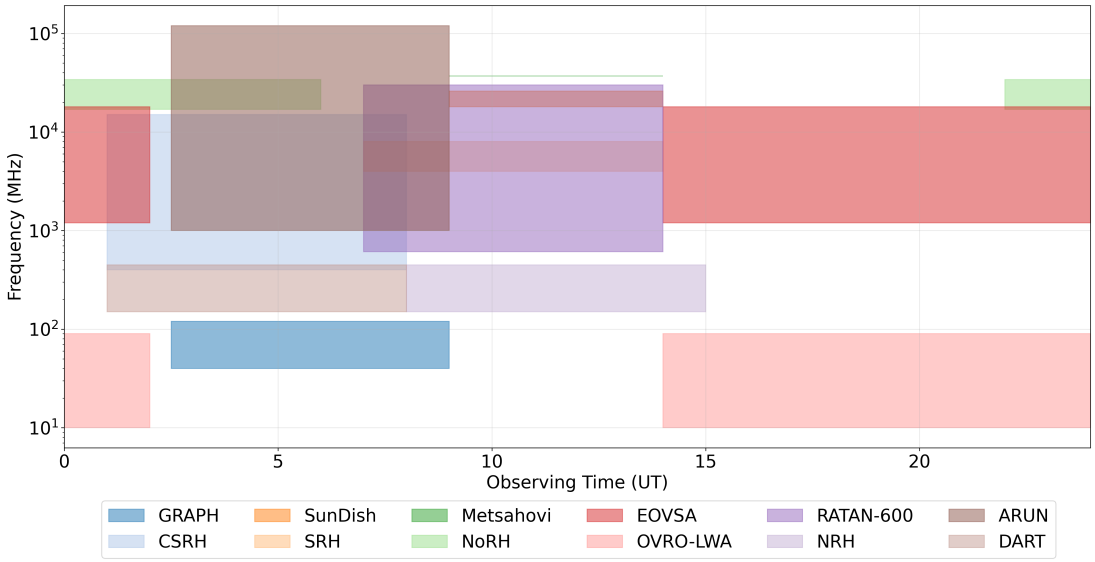

Figure 5: Time–frequency coverage for solar-dedicated radio interferometers and imaging arrays, plotted across UT and operating frequencies. These instruments are designed specifically for high-resolution imaging of the solar corona, mapping active regions, flares, CMEs, and coronal magnetic field topology. Shown are facilities such as GRAPH (40–120 MHz), CSRH / MUSER (0.4–15 GHz), SunDish (18–26 GHz), Siberian Radioheliograph (4–8 GHz), Metsähovi 37 GHz solar system, NoRH (17 & 34 GHz), EOVSA (1–18 GHz), OVRO-LWA, NRH (150–450 MHz), RATAN-600, ARUN (1–12 GHz solar imager) and others. Instruments crossing midnight (e.g., NoRH, EOVSA) are represented with wrap-around blocks. Collectively, these systems provide imaging across 0.04–37 GHz, offering unprecedented diagnostics of coronal magnetic fields, source heights, electron populations, and plasma dynamics from metric to millimeter wavelengths.

Together with NRH, several other instruments situated worldwide provide complementary solar radio imaging at microwave, decimetric, and metric wavelengths. Herein, we mention some of them. The SunDish project in Italy (Cagliari and Bologna) performs 2D spectropolarimetric imaging

[6] http://bass2000.obspm.fr/home.php

between 18 and 26 GHz with an angular resolution of approximately 1 arcmin, with weekly observations since 2018 (INAF, 2025). The Siberian Solar Radio Telescope (SSRT; see e.g. Grechnev et al., 2003) in Irkutsk, Russia, operates at 5.7 GHz and has been producing two-dimensional solar maps since 1997, making it one of the longest-running high-frequency imaging facilities. At metric wavelengths, the NRH (described above) provides dense snapshot imaging between 150 and 450 MHz using a 47-antenna interferometric array operating at up to ten frequencies. In India, the Gauribidanur Radioheliograph (GRAPH; Ramesh et al., 1998) observes at 40 – 120 MHz with a cadence of 0.25 s, generating daily solar images during local meridian transit (04:00–09:00 UT). Continuous observations have been available online since 2014. GRAPH is particularly valuable for tracking low-coronal Type III bursts, noise storms, and CME-associated sources at long wavelengths. The Daocheng Radio Telescope (DART) is a 1-km diameter, 313-element circular interferometric array operating at 150–450 MHz, designed for high-fidelity solar coronal imaging and complementary low-frequency radio astronomy observations in China. The Chinese Spectral Radioheliograph (CSRH)/ Mingantu Spectral Radio Heliograph (MUSER; Yan et al., 2021)(MUSER; Yan et al., 2021) operates from 0.4-15 GHz. The currently operational solar radio imaging instruments, together with their frequency ranges and typical observing times, are summarised in Figure 5.

At millimetric wavelengths, the Metsähovi Radio Observatory (MRO; Metsähovi Radio Observatory, 2019) in Finland observes at 37 GHz, providing daily full-sun maps since 1978. During the summer months, extended observing sessions of up to 14 hours per day are conducted, with each map requiring approximately 150 seconds of integration time. Microwave imaging at 17 and 34 GHz is performed by Nobeyama Radioheliograph (NoRH). NoRH has been decommissioned since 2020. An upcoming solar radio instrument in India, the Advanced Radio Telescope Udaipur Network for Solar and Space Weather Research (ARUN–SSW), operating in the 1–12 GHz range, is planned to be commissioned in the coming years [7]. NoRH was delivering high-cadence (0.1–1 s) imaging with spatial resolutions of $\sim 10''$ at 17 GHz and $\sim 5''$ at 34 GHz, including full Stokes I and V at 17 GHz and Stokes I at 34 GHz. Its continuous daily operation since 1992 has produced an unparalleled archive of flare and active-region microwave images.

In the United States, the Owens Valley Solar Array (EOVSA Gary et al., 2018) offers imaging capability across 39 frequencies between 1.2 and 18 GHz, enabling broadband mapping of gyrosynchrotron emission from flaring regions. EOVSA offers a raw frequency resolution of 122 kHz, corresponding to 4096 spectral channels, while the effective science-grade resolution is approximately 50 MHz [8]. The temporal sampling of the instrument is 20 ms, with a full spectral sweep completed every 1 s. Similarly, the RATAN-600 telescope in Russia (Korolkov and Pariiskii, 1979) provides one-dimensional scans at 112 frequencies spanning 0.7–18.2 GHz. Observations are typically carried out between 07:00 and 11:00 UT, producing 5–60 scans per day, with full Stokes I and V recorded at all channels. Together, these imaging facilities provide multi-frequency, multi-resolution views of the solar corona, enabling the detailed study of the flare energy release process and electron acceleration in the dense coronal plasma. Figure 6 shows the solar radio images in the metric range made with NRH.

[7] https://agu.confex.com/agu/agu25/meetingapp.cgi/Paper/1905282

[8] For EOVSA and OVRO-LWA, the effective observing windows are approximately 14:00–02:00 UT during summer and 16:00–23:30 UT during winter.

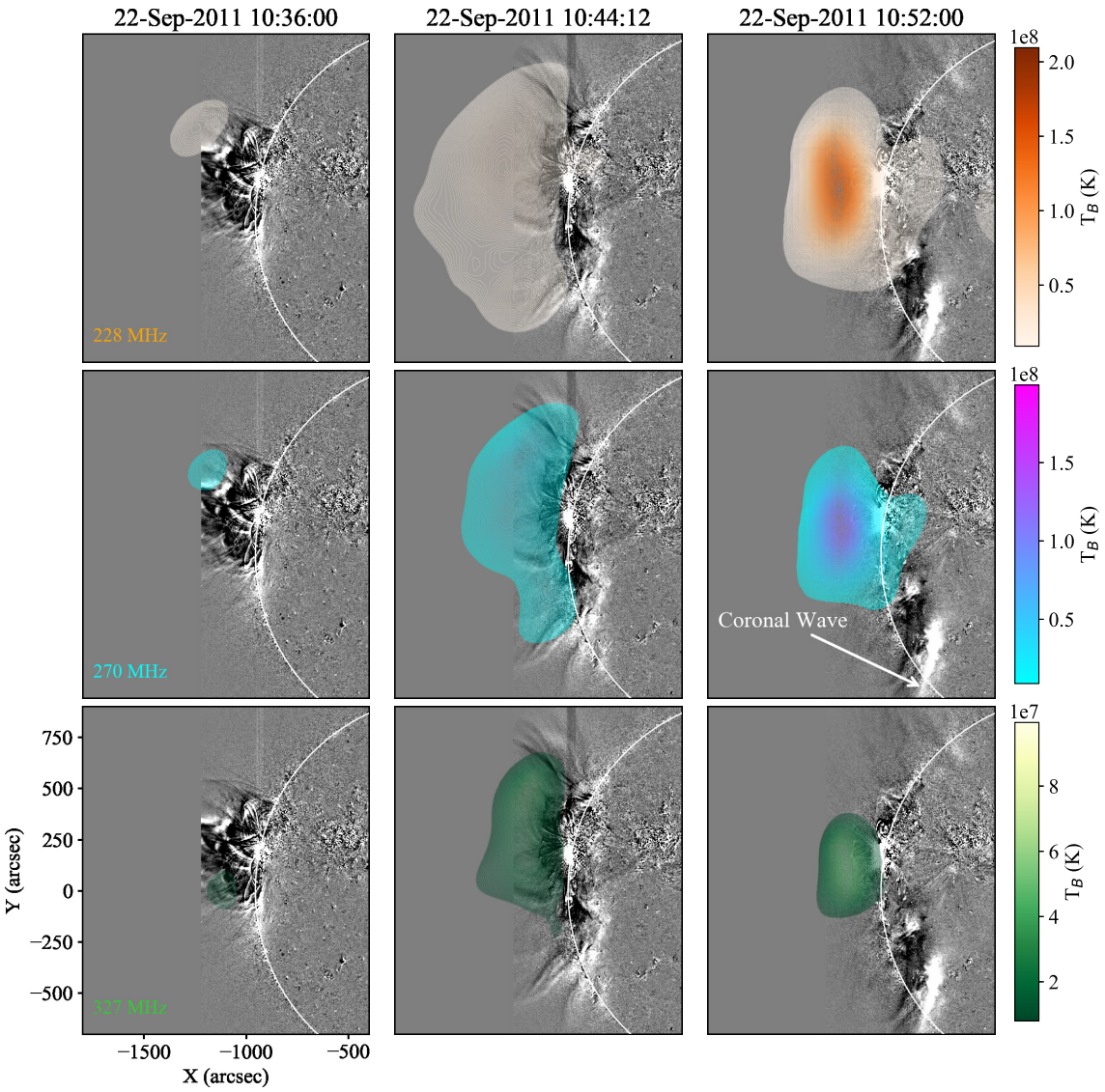

Figure 6: The radio sources from NRH (filled contours), during a type IV burst, overlaid over AIA 211 Å running-difference images. This figure is adapted from (Morosan et al., 2019).

Several powerful radio interferometers, although not dedicated solar instruments, regularly contribute to solar imaging through targeted campaigns or the dynamic allocation of observing time. The upgraded Giant Metrewave Radio Telescope (uGMRT; Gupta et al., 2017) in India, operating in the range of 150-1450 MHz, has been extensively used for high–fidelity imaging of solar transients due to its large collecting area and flexible correlator modes. The LOw Frequency ARray (LOFAR; van Haarlem et al., 2013) is another low frequency radio instrument. The LOFAR stations are spread across Europe, observing in the range 10–240 MHz, providing exceptional low–frequency coverage with dense core baselines suitable for coronal imaging. The Murchison Widefield Array (MWA; Tingay et al., 2013) in Australia, covering 80–300 MHz, routinely supports solar observations with snapshot uv–coverage that enables high–cadence imaging of rapidly evolving burst emission. At

microwave frequencies, the Karl G. Jansky Very Large Array (VLA; Perley et al., 2011) in the United States offers imaging from 1 to 50 GHz with full polarimetry, making it uniquely capable of probing gyrosynchrotron and gyroresonance sources in the low corona. MeerKAT (Jonas and Team, 2016) in South Africa, operating between 0.6–14 GHz, provides excellent sensitivity and dynamic range that have recently enabled new solar imaging experiments.

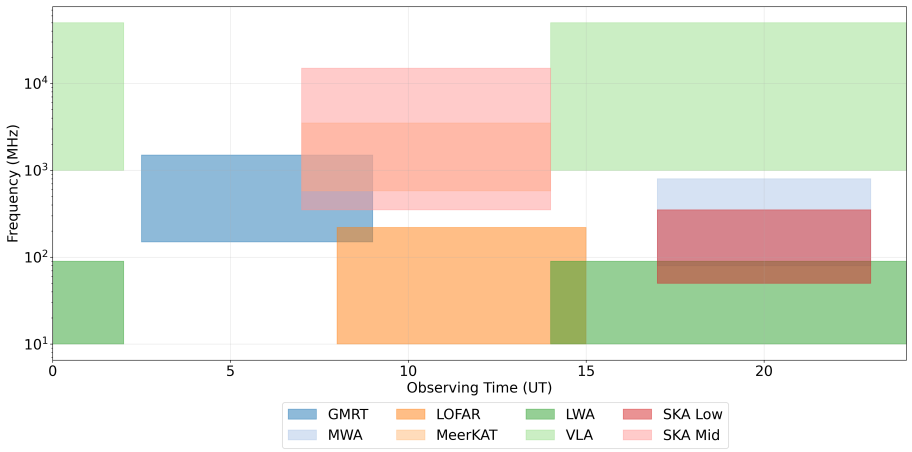

Figure 7: Observing windows and operational frequency bands for general-purpose radio interferometers that, while not solar-dedicated, routinely conduct solar imaging campaigns or support targeted observing modes. These include major low-frequency and microwave facilities such as GMRT, MWA, LOFAR, MeerKAT, LWA, VLA, SKA-Low, and SKA-Mid. Their wide instantaneous bandwidths and flexible correlator architectures enable high-dynamic-range imaging of the Sun on demand, though scheduling is constrained by competition with non-solar programs. Frequency ranges span 10 MHz to 50 GHz, allowing these arrays to capture a wide variety of solar radio phenomena from low-coronal plasma emission to gyrosynchrotron and gyroresonance processes. These instruments complement solar-dedicated arrays by providing superior sensitivity, large collecting areas, and advanced imaging fidelity, thereby extending the global solar radio observing capability into professional radio astronomy infrastructures.

Next–generation facilities will further expand these capabilities. The Long Wavelength Array (LWA; 10–88 MHz) in the United States provides ultra–low frequency imaging suited for coronal plasma processes (Henning et al., 2010), while the Square Kilometre Array (SKA)—comprising SKA-Low (50–350 MHz) in Australia and SKA-Mid (0.35–15.3 GHz) in South Africa (see e.g., Henning et al., 2010; Nakariakov et al., 2015; Dewdney et al., 2017) will deliver wideband, high–dynamic–range imaging spectropolarimetry across nearly two decades of frequency. Although these observatories prioritise non-solar astrophysical science, their large collecting areas, sophisticated correlators, and flexible scheduling make them invaluable contributors to solar radio research, complementing dedicated solar arrays and significantly extending the global imaging capability of the heliophysics community. The currently operational non-solar radio imaging instruments, occasionally used for solar observations, together with their frequency ranges and typical observing times, are summarised in Figure 7.

2.4 Direction finding observations

Mapping the positions of radio sources at frequencies below approximately 10 MHz is not possible with interferometric arrays, i.e., with ground-based instruments, due to the ionospheric cutoff. To

estimate the locations of radio sources at large wavelengths and far from the Sun, one-dimensional (1D) electron density models (e.g., Newkirk, 1961b; Saito et al., 1977; Leblanc et al., 1995) have been employed for decades when no other observations or methods were available. The 1D density models assume radial symmetry, and without the spatial information, they can provide only radial distance of the radio source positions (see e.g. Knock and Cairns, 2005; Magdalenić et al., 2008; Alissandrakis, 2020). On the other hand, the direction-finding (DF) observations from space-based instruments available over the last few decades provide significantly more information on the source locations than only the radial distance of the source. The direction finding observations are the only way to obtain the position of the radio sources in the 3D space, without using additional assumptions or simplifications see e.g. Krupar et al., 2012; Magdalenić et al., 2014; Jebaraj et al., 2020. The propagation path of solar radio bursts obtained using radio triangulation is shown in Figure 8.

Direction-finding observations are single-spacecraft measurements allowing us to determine the direction of arrival of an incident radio wave (Cecconi and Zarka, 2005). Spacecraft equipped with radio antennas measure properties of incoming radio waves, such as intensity, polarization, and the direction of arrival. The direction is typically expressed in terms of colatitude and azimuth relative to the spacecraft frame. This allows us to estimate the wave's direction in space, i.e. a line of sight to the radio source. Depending on the type of spacecraft, i.e., spinning (Wind) or three-axis stabilized (STEREO, SolO, PSP), different techniques are used to estimate the direction finding parameters (Fainberg and Stone, 1974; Cecconi and Zarka, 2005; Krupar et al., 2012). A single spacecraft can only provide the direction of the wave vector. In order to obtain accurate three-dimensional (3D) radio source positions, the triangulation method using DF measurements from two or more widely separated spacecraft needs to be employed. The intersection region of the two wave vectors determines the source location of the radio emission (Reiner et al., 1998; Magdalenić et al., 2014; Krupar et al., 2016; Jebaraj et al., 2020; Deshpande et al., 2025).

2.5 Space-based solar radio observatories

As introduced in the previous section, in order to overcome the ionospheric cutoff, the frequencies below ~10 MHz need to be observed by the space-based instruments. All types of solar radio bursts, except type I bursts, are observed at these low frequencies. They often, but not necessarily, start in the metric range and continue to the kilometric wavelengths. The radio bursts observed by space-based instruments provide important information on the characteristics of the interplanetary medium, which is essential in the validation of the space weather models and in the operational space weather forecasting (see e.g. Magdalenić et al., 2014; Valentino and Magdalenić, 2024; Deshpande et al., 2025, and references therein).

The first ever solar radio observations by space-based instrument was performed by RAE-1 (Radio Astronomy Explorer; Alexander et al., 1970). Dynamic spectra obtained by the radiometer spanned a frequency range of approximately 0.2 to 10 MHz. Since then the missions such RAE-2 (Alexander et al., 1975), Helios 1 and 2 (Porsche, 1977, 1979), Voyager 1 and 2 (Stone et al., 1977, 1979), ISEE 1, 2 and 3 (Riedler and Krüger, 1977; Ogilvie et al., 1978), and Ulysses (Meeks and Massey, 1990) largely contributed to the spectroscopic observations.

Modern space-based observations have undergone significant improvements since these early mis-

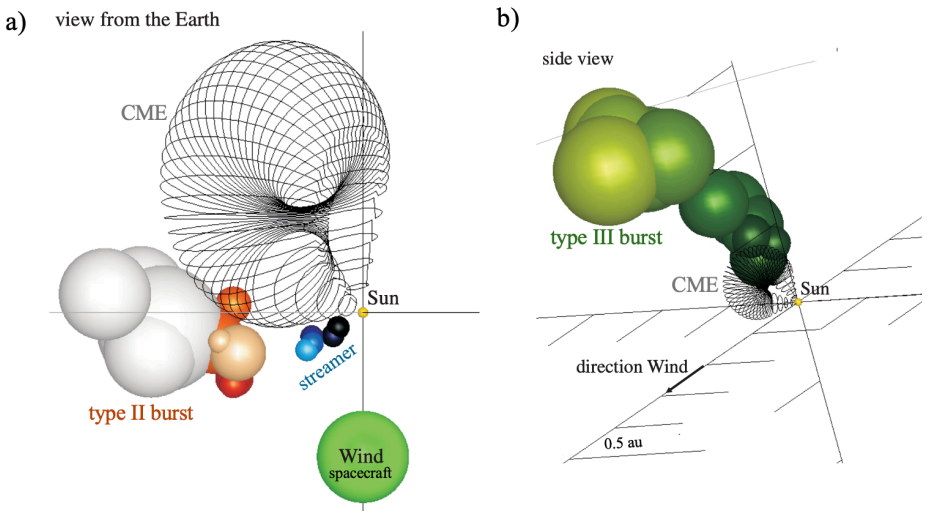

Figure 8: The propagation path of the type II and type III radio bursts obtained using radio triangulation (panels a and b), respectively. The studied radio event was associated with the CME/flare event observed on March 05, 2012. The size of the colourful spheres is half the distance between the two wave vectors obtained using the direction finding data. The sources are colour-coded, with the lighter colour corresponding to the lower observing frequency pairs. The black grid croissant represents the 3D reconstruction of the CME flux rope in the studied event, while blue spheres represent the 3D reconstruction of the nearby streamer. (Figure is adapted from Magdalenić et al., 2014).

sions. After its launch in 1994, Wind/Waves (Bougeret et al., 1995) provides continuous observations of the dynamic spectra from the L1 Lagrange point. It also offers thermal noise observations and DF measurements. STEREO/SWaves (Kaiser et al., 2008; Bougeret et al., 2008) consists of two identical spacecraft, STEREO-A and STEREO-B, offering multi-point observations around the Sun at approximately 1 au, with STEREO-B observations available until October 2014. In addition to its broadband dynamic spectra, STEREO/SWAVES provides DF measurements. The novel spectroscopic observations by Parker Solar Probe (PSP; Fox et al., 2016), Solar Orbiter (SolO; Müller et al., 2020) and Bepi Colombo provide high frequency and time resolution observations. These novel missions explore the inner heliosphere from various vantage points near the Sun. They observe the Sun from close distances, providing an opportunity to study solar radio emissions near their source regions. BepiColombo, PSP, and Solar Orbiter also provide thermal noise measurements. Additionally, PSP and Solar Orbiter are equipped with DF capabilities. Table 1 presents a summary of the major space-based solar radio instruments operating from 1970 to the present, highlighting their frequency coverage, measurement capabilities, and mission context. While the DF measurements can be used to obtain 3D radio source positions (Krupar et al., 2014a,b; Magdalenić et al., 2014; Jebaraj et al., 2020; Deshpande et al., 2025) as mentioned in Section 2.4, multi-spacecraft

Table 1: Summary of major space-based solar radio instruments from 1970 to present.

Mission / Instrument	Freq. Range (MHz)	Measurement	Years	Notes
Currently Operating				
Wind/WAVES	0.02–13.825	Spectrometer + DF	1994–	Reference for IP bursts
STEREO-A/SWAVES	0.0025–16	Spectrometer + DF	2006–	Full GP capability
Parker Solar Probe/RFS	0.01–19.2	Radio + E-field + DF	2018–	Closest to Sun
Solar Orbiter/RPW	0.0005–16	Radio + DF	2020–	Tri-axial antennas
BepiColombo Mio/PWI	<0.01	Plasma waves	2018–	LF electric field only
Historical Missions				
STEREO-B/SWAVES	0.0025–16	Spectrometer + DF	2006–14/16	Limited post-recovery
Ulysses/URAP	0.001–1	Radio + plasma waves	1990–2009	High-latitude mission
ISEE-3 (ICE)/RAE	0.03–2	Solar radio	1978–1997	Early DF
Helios A/B	up to 1	Radio + plasma waves	1974–1986	Inner-heliosphere data
IMP-6/IMP-8	0.03–1.2	Solar radio	1970–2001	Early space dynamic spectra
Voyager 1/2 PWS	10^{-5}–0.056	Plasma waves	1977–	IP shocks, not bursts

spectroscopic observations can provide 2D information, i.e., radio source trajectory (see e.g. Musset et al., 2021; Badman et al., 2022).

3 Solar Radio Observations

3.1 Active Sun observations

3.1.1 Types of Solar Radio Bursts

Solar radio bursts can be produced by energetic processes in the solar corona, such as solar flares and coronal mass ejections (CMEs), but they are also frequently observed in the absence of large eruptive events. These bursts occur following the acceleration of electron beams that can, in turn, generate emission at radio wavelengths most frequently through the plasma emission mechanism (see e.g. Klassen et al., 2002, and the references therein). Solar radio bursts are classified based on their shape and characteristics in radio dynamic spectra as type I, II, III, IV and V (Wild, 1950; Wild et al., 1963; Suzuki and Dulk, 1985). Different types of solar radio bursts and their characteristic signatures in the dynamic spectrum are shown in Figure 9.

Type I Bursts: Metric type I solar radio bursts are observed in dynamic spectra as narrowband (a few MHz), generally non-drifting bursts of short duration, typically about 0.1 s. When observed in single-frequency records, they appear as numerous "spiky" bursts of much higher intensity (several

tens of sfu) than the intensity of the underlying background continuum. They usually occur in chains or small groups of bursts. Type I bursts are embedded in a weak, slowly varying continuum of emission, and the burst complex is referred to as a noise storm. In the metric-decametric wavelength range, type I bursts transition into type III bursts(Mugundhan et al., 2018). The characteristics of individual bursts in the storm are generally similar to those found in chains or groups. Noise storms can last from a few tens of minutes to several days. Long duration is one of the main characteristics that distinguishes storms from other types of solar radio emissions (type II bursts or isolated type III bursts). Type I storms are generally associated with continuous reconnection above complex active regions (Gary and Keller, 2004), rather than directly with flaring activity. One possible mechanism for their generation is the avalanche model (Mercier and Trottet, 1997). The frequency range in which they appear indicates that the emission mechanism is probably fundamental-frequency plasma emission. Some of the very important characteristics of type I storms, e.g., high brightness temperature and strong o-mode polarization (when the source is on the disk), can be explained by this hypothesis (for review see e.g. McLean and Labrum, 1985). It should be stressed that type I bursts are the most common type of solar radio bursts in metric wavelengths, but they are not very often studied.

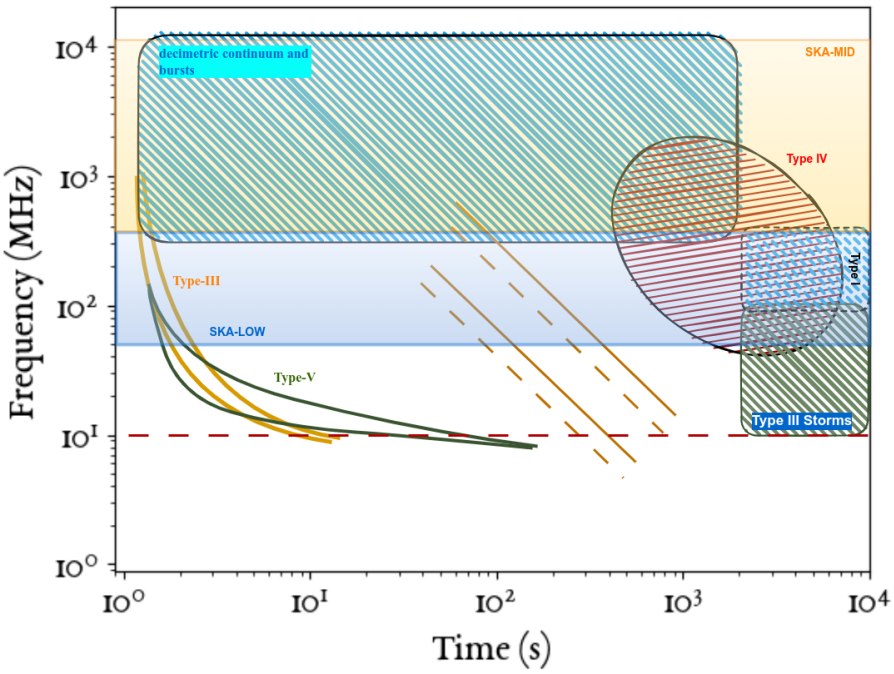

Figure 9: Different types of solar radio bursts and their characteristic signatures in the dynamic spectrum. Type II bursts are slowly drifting emission lanes known as shock wave signatures. The rapidly drifting type III bursts are produced by very fast electron beams. Type IV bursts present broadband, long-duration continuum often associated with the lift-up of the CME. Type I noise storms appear as narrowband, short-lived bursts sometimes superimposed on a weak continuum background.

Type II Bursts: Type II bursts are slowly drifting emission lanes observed at metric to decametric wavelengths in dynamic spectra at the fundamental and/or harmonic of the plasma frequency (Mann et al., 1996; Nelson and Melrose, 1985a; Kumari et al., 2023). The fundamental and harmonic

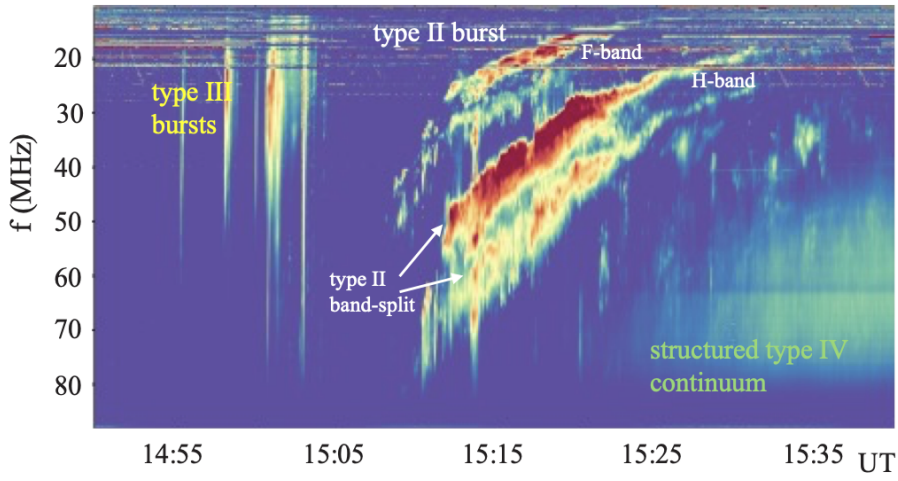

Figure 10: Dynamic spectrum shows typical radio bursts observed during an eruptive event, i.e. type II and type III bursts and continuum type IV radio emission. In addition to different types of bursts, the fundamental and harmonic band (F- and H-band) of type II bursts are marked, together with the two band-split lanes of type II. This radio event was associated with the CME/flare event on August 25, 2014. Adapted from Magdalenić et al. (2020).

emission bands often show a split, so-called band-split (e.g. Smerd et al., 1975; Vršnak et al., 2001, 2002; Magdalenić et al., 2002; Kumari et al., 2017b, 2019) and numerous fine structures (e.g. Magdalenić et al., 2020, see Figure 9). For example,'herringbones' are type II fine structures stemming from a type II 'backbone', characterized by their fast drift towards either low or high frequencies (Holman and Pesses, 1983; Cairns and Robinson, 1987; Cane and White, 1989; Magdalenić et al., 2002). Herringbones sometimes also occur without a type II backbone (Holman and Pesses, 1983; Morosan et al., 2019). A broad variety of fine structures, with different morphologies and drifts, comprising the emission lanes of type II bursts, was recently reported by Magdalenić et al. (2020) and Zhang et al. (2024a).

Type II bursts are generally considered as the radio signatures of propagating shock waves in the solar corona, with the majority of them being CME-driven (e.g. Smerd, 1970; Mann et al., 1996; Carley et al., 2013; Kumari et al., 2017a; Zucca et al., 2018; Morosan et al., 2019; Umuhire et al., 2021; Kandekar and Kumari, 2025) and only occasionally of different origin, like e.g. flare generated (see e.g. Magdalenić et al., 2008; Vasanth, 2024). Herringbones, fine structures of type IIs represent signatures of individual electron beams escaping the shock, sometimes in opposite directions (Zlobec et al., 1993; Carley et al., 2013; Morosan et al., 2019). Unlike the backbone of type II bursts, herringbones have only been imaged on rare occasions (Carley et al., 2013; Morosan et al., 2019, 2022a) and were found to closely follow the propagation of extreme-ultraviolet (EUV) waves in the low corona and fast lateral expansion of the CME at higher altitudes. The EUV wave represents a fast-mode wave or shock wave that propagates in the low solar corona ahead of the expanding CME (Long et al., 2008; Kienreich et al., 2009; Warmuth, 2015; Majumdar et al., 2021). Morosan et al. (2022a) suggested that the close association of herringbones with the EUV wave and CME expansion points to the formation of a large-amplitude wave that undergoes steepening into a

shock during the onset of the CME eruption (Vršnak and Lulić, 2000a,b).

Several recent studies have focused on determining the origin of band splittings in coronal type II radio bursts, utilising novel high-spatial resolution observations. As mentioned earlier, band-split is a characteristic of type II bursts where emission lanes consist of two or more bands of similar drift rates and morphology (e.g. Vršnak et al., 2001; Magdalenić et al., 2020). Recently available high-resolution radio imaging observations in the metric range revealed that these two bands originate in neighboring but distinct regions upstream of the shock (e.g. Bhunia et al., 2023; Zhang et al., 2024b; Normo et al., 2025). This is contrary to the scenario proposed by Smerd et al. (1975), suggesting that these bands would be emitted simultaneously upstream and downstream of the shock. On the other hand, the study of interplanetary type II radio bursts (e.g. Vršnak et al., 2001) clearly shows that, at least in the case of some type II bursts, the band-split is most probably emission from the upstream and downstream shock regions, in accordance with hypothesis by Smerd et al. (1975). These results indicate that the split of the type II emission bands might not necessarily always have the same origin, in particularly when different plasma regimes such as low corona and interplanetary space, are considered.

Type III Bursts: Type III radio bursts are the most frequently observed type of radio burst in dynamic spectra. They appear as fast-drifting structures often spanning the full frequency range, all the way from the gigahertz to kilohertz range. They are signatures of fast electron beams traveling along open or quasi-open magnetic field lines. The type III generating energetic electrons ($\sim$ 5 – 50 keV) propagate with speeds of fraction of the speed of light often reaching as large speeds as ~0.3 c (Reid and Ratcliffe, 2014). The associated type III radio emission is generated through the plasma emission mechanism (Zheleznyakov and Zaitsev, 1968; Melrose, 1974). In this nonlinear process, one of the very frequently appearing instability, so called a bump-on-tail instability generates Langmuir waves which subsequently undergo coalescence and/or scattering, producing radio emission at the fundamental plasma frequency or its harmonics (e.g., Robinson, 1978).

Type III radio bursts observed at GHz to few hundred of MHz range are frequently associated with X-ray emission sources (Kane, 1972; Arzner and Benz, 2005; Reid and Kontar, 2017a; James and Vilmer, 2023). Studying both types of emissions provides information about the acceleration sites of the associated electron beams (see e.g. Reid et al., 2011; Bhunia et al., 2025). The type III electron beams often, but not always, propagate into the outer corona along open magnetic field lines. Electron beams that do not escape into the outer corona and instead propagate along closed loop structures are often observed as U- or J-bursts (Reid and Kontar, 2017b). Such bursts are produced when coronal loops are dense and extended enough to support the instability required for Langmuir wave generation (Reid and Ratcliffe, 2014).

Metric type III radio bursts have been studied for many decades. Dynamic spectra show frequency drift rates of type IIIs to be typically of about 10 MHz/s at 60 MHz, and scale approximately as $df/dt = 0.067 f^{1.23}$ [MHz] (Zhang et al., 2018). The type III drift rates can serve as a proxy for the estimation of the speed of the associated electron beams. By applying coronal electron density models, one can relate the observed emission frequency to height in the corona and thus trace the structure of the coronal electron density (see e.g., Dabrowski et al., 2021). Imaging of type III

bursts helps trace the propagation path of the emission and, indirectly, the electron beams themselves. Radio sources at each frequency correspond to different heights in the corona, enabling the mapping of coronal plasma parameters. The source sizes of type III bursts often, but not necessarily always, increases with decreasing frequency, reflecting beam broadening and propagation effects (Steinberg et al., 1985; Saint-Hilaire et al., 2012a). Recent study of interplanetary type III bursts, by Deshpande et al. (2025) show rather steady trend of the type III source sizes than the clear increase.

Type III radio bursts are among the most intense structures of all SRBs. Their intensity is, similarly to type II radio bursts, observed to increase up to approximately 1 MHz and then decrease towards lower frequencies. Type III bursts typically continue down to very low frequencies, around 0.1 MHz, reflecting the propagation of the electron beams into the interplanetary medium. However, not all bursts extend that far. Type III bursts ending frequency depends on the radial expansion of the guiding flux tube, the initial conditions of the electron beam, and strong density fluctuations that reduce wave growth (Reid and Kontar, 2015). Type III bursts propagate from high-density to low-density regions through an inhomogeneous ambient plasma, and as a consequence they often exhibit fine frequency structures in the dynamic spectra, typically appearing as horizontal striae with a fractional bandwidth of ∼0.1 (see e.g. Reid and Kontar, 2021; Jebaraj et al., 2023b). Fine structures have been studied for a long time in the metric range (Cairns and Robinson, 1987), and recent work has also reported similar structures at very low frequencies (Jebaraj et al., 2023b; Krupar et al., 2025). These striations are believed to arise from strong density turbulence in the background plasma (Mugundhan et al., 2016, 2017). Observations show that the striae are most prominent in the fundamental component, indicating that it is more sensitive to density fluctuations (Kontar et al., 2017; Sharykin et al., 2018; Reid and Kontar, 2021; Zhang et al., 2020). Fundamental and harmonic components of type III bursts are difficult to observe simultaneously, in particular in the metric range, consequently clear examples of the both bursts component are not very often reported (Wild et al., 1959; Mann et al., 2018; Melnik et al., 2019; Zhang et al., 2020; Vocks, C. et al., 2023). Recent high frequency/time resolution observations from PSP have shown that both components can indeed be detected in the interplanetary range, with the fundamental component being dominant most of the time (Jebaraj et al., 2023a; Chen et al., 2024).

Type IV Bursts: Type IV bursts are long-duration, broadband continuum emissions associated most commonly with CMEs (Webb and Howard, 2012; Robinson, 1986; Kumari et al., 2021; Kumari, 2022; Mohan et al., 2024). These emissions can be observed over a wide range of wavelengths spanning from decimetric to metric wavelengths (Pick, 1986). Based on their appearance in the dynamic spectrum, they are divided into two main sub-categories – moving type IV bursts (IVm) and the stationary type IV bursts (IVs) (Boischot, 1957). Although historically number of different subcategories of the type IV continuum were presented by Kundu, last few decades mostly two main sub-categories are discussed. While the envelope of the IVm bursts show frequency drift, indicating an outward motion of the associated radio source from the Sun, the IVs bursts do not show any drift, indicating a stationary radio source (Pick, 1986). Schematic examples of IV bursts are shown in Figure 9. These bursts can originate from either stationary or moving radio sources (for a review, see Bastian et al., 1998).

The source of the stationary continuum, so called IVs burst remains rather static in the corona

above the active region or in the leg of the post-flare loop systems, and are typically interpreted as emissions from the non-thermal electrons present in association with a flare and the lift-off of a CME (see e.g. Salas-Matamoros and Klein, 2020). Consequently, type IVs continuum is often considered as a key element to understand the reconstruction in the solar corona after the flare/CME events. Studies of the type IV sources show that the basic source structure of IVs bursts is columnar, i.e., the sources at different frequencies align, at the leg(s) of the erupting flux rope (see e.g. Kai et al., 1985; Salas-Matamoros and Klein, 2020). High brightness temperature (typically $\geq 10^9 K$) and strong left-handed circular polarization (near 100%) suggest the IVs to originate through the plasma emission mechanism (Melrose, 1975). However, recently some studies report that the emission mechanism of long-duration IVs continuum is an electron cyclotron maser (ECM) process (Liu et al., 2018).

Bastian et al. (2001) were the first to report the existence of a 'radio CME', observed as an ensemble of loop structures imaged by the Nançay Radioheliograph. The loops extended to distances of up to 3 $R_\odot$ at 164 MHz and were made visible at radio wavelengths by synchrotron-emitting electrons. Radio imaging and spectroscopy indicate that these moving sources can mark confined populations of accelerated electrons behind the CME or inside CME cores and erupting filaments (e.g. Morosan et al., 2019; Vasanth et al., 2019; Morosan et al., 2021; Klein et al., 2024) and in rare cases, these electrons can be trapped inside the CME(Bastian et al., 2001; Chen et al., 2025). Some IVm bursts can also be composed of fine structures, i.e., narrow-band, highly polarized and/or rapidly varying emission, (Gary et al., 1985; Vasanth et al., 2019; Morosan et al., 2020) considered to be generated by the plasma emission mechanism.

Table 2: Summary of the types of solar radio bursts.

Type	Characteristics	Duration	Frequency Range	Associated Phenomena
I	Short, narrow-band bursts occur in large numbers, usually with an underlying continuum.	Single burst: ~1 s; Storm: hours–days	80–200 MHz	Active regions, flares, eruptive prominences
II	Slow-drift bursts, often with strong second harmonic.	3–30 min	Fundamental: 20–150 MHz	Flares, proton emission, MHD shock waves
III	Fast-drift bursts occur singly, in groups, or in storms (with or without continuum). Often with a second harmonic.	Single: 1–3 s; Group: 1–5 min; Storm: minutes–hours	10 kHz–1 GHz	Active regions, flares
IV (Stationary)	Broadband continuum with fine structure.	Hours–days	20 MHz–2 GHz	Flares, proton emission
IV (Moving)	Broadband continuum with slow frequency drift.	30 min–2 h	20–400 MHz	Eruptive prominences, shocks
V	Smooth, short-lived continuum; follows type III; never occurs alone.	1–3 min	10–200 MHz	Same as Type III bursts

Type V Bursts: The most rarely observed radio bursts are type V solar radio bursts. This broadband continuum emission occurs at frequencies generally lower than 200 MHz. It typically appears immediately following a group of Type III bursts and lasts from about one to a few minutes, most often at metric–decametric frequencies (commonly below ~120 MHz). About 45% of the type V events at 25 MHz accompany type III groups (Daene and KrüGER, 1966), though this fraction likely reflects instrumental sensitivity. Combined type III/V activity correlates more strongly with hard X-ray flares than single type III bursts, indicating that they may trace more energetic particle acceleration (Stewart, 1978). Some cases show a temporal gap between the two type IIIs and V, forming detached events.

Whether Type V bursts are a genuinely separate class or a manifestation of blended, unresolved type III activity remains contentious (Morosan et al., 2022c). Imaging data show that Type V sources occur at comparable coronal heights to Type III sources and show similar displacement in source position with frequency to that of the type IIIs, but their emission regions are often displaced by several tenths of a solar radius. They also decay more slowly and radiate less directionally. Associations between U-shaped type III trajectories and subsequent type V continua indicate that closed magnetic structures can play a role in the generation of these bursts. Their circular polarization is generally weak ($\geq$ 10%) and often opposite in sense to the preceding type III emission, especially when the type III and V sources are spatially well separated (Dulk et al., 1980).

The emission mechanism of type V bursts remains unresolved. Though the emission mechanism was proposed to be gyrosynchrotron of the type III emitting electron beam (Wild et al., 1959), it was rejected early due to spectral inconsistencies. Plasma emission from electrons redistributed or confined in coronal loops has been widely discussed (Weiss and Stewart, 1965; Zheleznyakov and Zaitsev, 1968). However, beam evolution models, ranging from gap-type distributions (Melrose, 1975) to upper-hybrid wave coalescence and ECM-related scenarios (Winglee and Dulk, 1986), have also been proposed. Several instability-driven scattering mechanisms, including whistler scattering (Melrose, 1974), ion-cyclotron–driven isotropization (Benz, 1974), and the electron firehose instability (EFI) (Paesold and Benz, 1999, 2003), may produce the anisotropies required for coherent emission. Recent in situ detection of EFI-like signatures (Cozzani et al., 2023) lends support to these ideas. Overall, Type V bursts appear to involve electron populations that evolve differently from those producing narrow beams, which are associated with Type III bursts; however, high-resolution observations are still needed to establish their exact nature.

Figure 9 shows the different types of solar radio bursts and their characteristic signatures in time–frequency space. Table 2 summarises the different types of solar radio bursts, their characteristic signatures, and the physical emission mechanisms associated with each class.

3.2 Probing Coronal Plasma with Solar Radio Bursts

Solar radio bursts provide a powerful remote probe of the electron beams and plasma conditions in the solar corona: their brightness, apparent size, and spectral properties encode how energetic electrons propagate, interact with turbulent plasma, and convert their energy into coherent radio emission (Dulk, 1985).

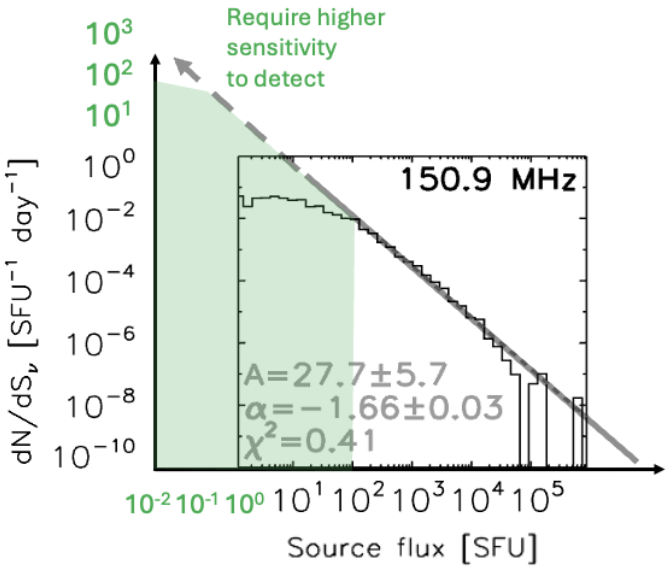

Figure 11: Differential distribution of solar radio burst flux densities at 150.9 MHz (Saint-Hilaire et al., 2012b). The solid line indicates a power-law fit to the observed events, while the shaded region indicates the large, currently unobserved population of weak bursts that would require higher sensitivity instruments to be clearly detected.

3.2.1 Brightness

A central question in the coronal heating problem is whether the energy released by numerous small radio bursts can rival, or strongly contribute to, that of the rarer, very bright events. This can be addressed statistically by measuring the distribution of burst fluxes. Figure 11 shows the differential number distribution of solar radio burst flux densities dN/dS_ν at 150.9 MHz. The events, observed over several decades, follow a power-law in flux, with a best-fit slope $\alpha \simeq -1.66$. The shaded region indicates the regime where the burst fluxes fall below the current detection threshold. In this range, the expected occurrence rate of radio bursts steeply rises, but the individual bursts remain unresolved in the dynamic spectra. If the power-law continues into this low-flux domain, the cumulative energy carried by the undetected population may be comparable to (or even exceed) that of the bright, easily observed bursts. Improving the instrumental sensitivity and dynamic range is therefore essential for quantifying the true burst energy budget and assessing its contribution to coronal heating.

3.2.2 Radio Bursts Source size

The apparent size of a radio burst encodes crucial information about the characteristics of the coronal plasma. At frequencies < 300 MHz, radio waves are notably affected by scattering due to the density fluctuations along the line of sight, which then can broaden and distort the intrinsic source size and structure. High-resolution imaging observations over a wide range of frequencies enable us to measure how the source size and morphology evolve with height in the corona, allowing us to separate intrinsic source properties from propagation effects (Mondal et al., 2025). Comparison of observations and forward models of radio-wave scattering and refraction can, to a certain extent,

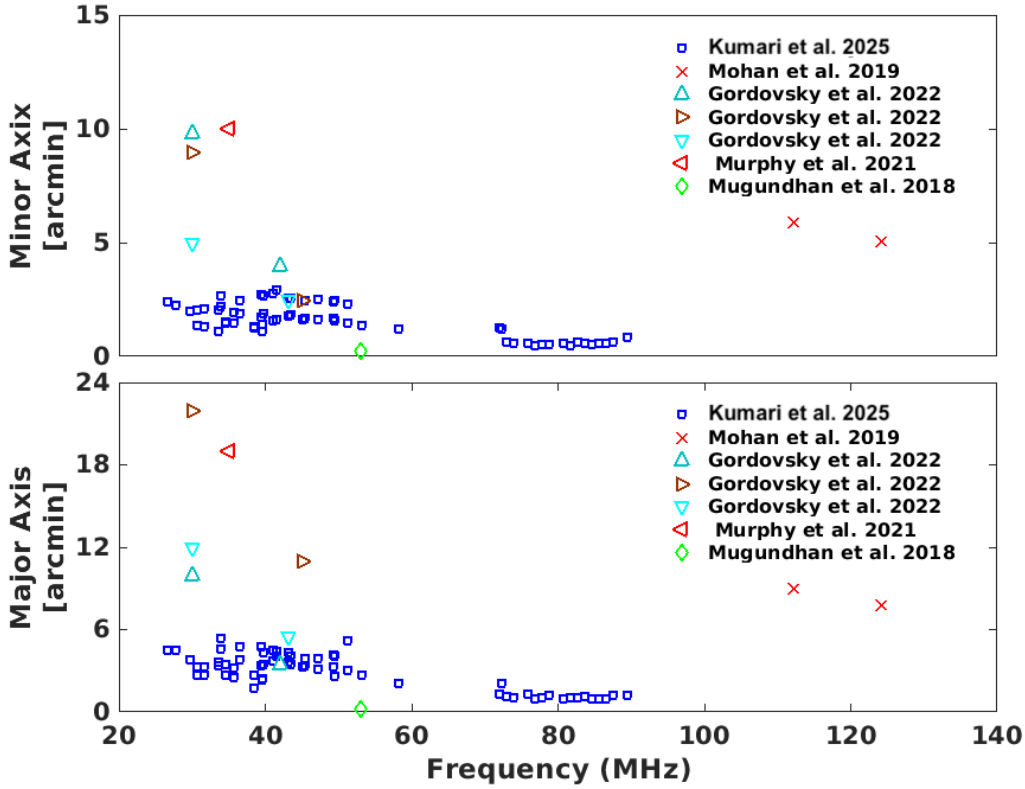

Figure 12: Combined plot of radio burst source sizes from a number of previous studies. 'Blue' squares present the source sizes for fundamental-harmonic lanes of three type II radio bursts. Notably, the source sizes (both minor and major) obtained in the present study are smaller than those in all previous studies using different instruments and observation modes (except Mugundhan et al. (2018)). The figure has been adopted from Kumari et al. (2025).

constrain the amplitude and spatial spectrum of coronal density fluctuations, as well as the physical size of the emitting region.

Using LOFAR's large baselines, notable advances have been made in quantifying the source sizes of type II radio bursts. Figure 12 from Kumari et al. (2025) presents a combined plot of the sizes of radio bursts observed in various studies to date. These studies include type II bursts observed with both LOFAR's interferometric mode with a maximum baseline of 80 km (Kumari et al., 2025) and LOFAR's tied-array beam observations of type II radio bursts with a baseline of ~2 km (Gordovskyy et al., 2022). Other radio burst source sizes are also included, such as type III bursts observed with MWA with a baseline of ~3 km (Mohan et al., 2019), type III radio bursts observed with LOFAR's interferometric mode (Murphy et al., 2021) and VLBI (200 km) of a noise storm (Mugundhan et al., 2018). The source sizes obtained by (Kumari et al., 2025) are smaller than those in previous studies except that of Mugundhan et al. (2018), where the baseline was the largest (≈ 200 km). Another study by Morosan et al. (2025a) demonstrated that increasing the interferometric baseline for snapshot imaging with LOFAR also decreases the size of the observed sources, allowing for

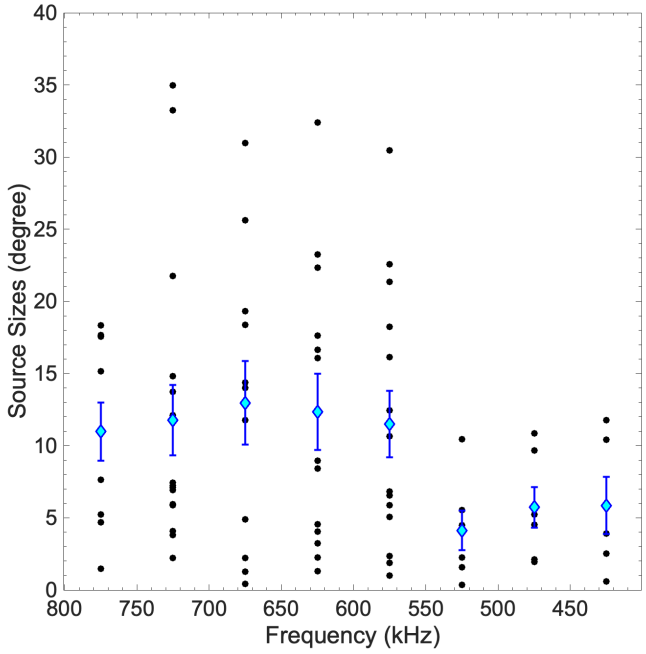

Figure 13: Variation of radio source sizes with frequency for interplanetary type III radio bursts from the recent study by Deshpande et al. (2025). The blue error bars map the standard deviation estimated from bootstrapping and the cyan colored points represent the mean calculated using the bootstrapping method. Adapted from Deshpande et al. (2025).

more details to be resolved in the images. Additionally, an elongated radio source was resolved into two separate components when using LOFAR's longer baselines. These spatial resolution observations also allowed for the determination of rippling scales at the shock front of the order of $\sim 10^5$ km (Morosan et al., 2025b).

The recent study of interplanetary type III radio burst sources by Deshpande et al. (2025) employs direction-finding observations and the radio triangulation method in estimating the radio source sizes. The authors demonstrate that type III source sizes are relatively constant (Fig. 13) in the frequency range of 800 MHz to 400 MHz. This suggests that scattering effects are likely not dominant in this plasma regime. On the other hand, the authors also estimated level of the density fluctuations using independently the in situ observations by PSP, and found that the level of the density fluctuations is rather low, of the order of 5 - 6 % which is in accordance with the rather stable type III radio source sizes obtained with the radio triangulation method.

3.2.3 Emission mechanism

The radio emission mechanism links the observed properties of the bursts to the underlying energetic particles and plasma conditions. Most metric and decametric solar radio bursts are produced by coherent plasma emission. The nonthermal electron beams or unstable electron distributions drive Langmuir waves, which are converted into escaping electromagnetic radiation at the local plasma frequency and/or its harmonics. The resulting spectra is of a narrow bandwidth, very high brightness temperatures, and characteristic frequency–time drift rates that reflect the electron propagation

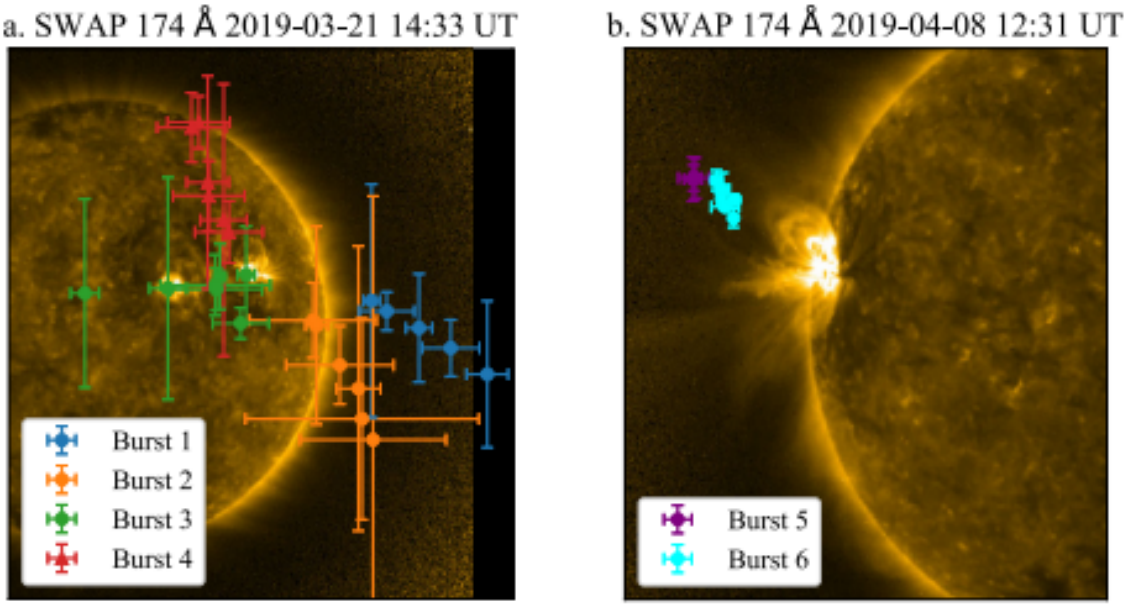

Figure 14: Centroid positions of solar radio bursts derived from tied–array imaging with a low–frequency radio interferometer, overlaid on an EUV image of the Sun. The centroids obtained at multiple frequencies reveal the spatial evolution of burst source regions through the corona. (Morosan et al., 2022b).

through the coronal plasma of a changing density. By combining information on the spectral characteristics of the bursts such as e.g. drifts, band split, fine structures characteristics and polarization level, with the constraints on source position and size obtained from imaging observations, we can distinguish between different emission scenarios. That allows us to infer key parameters of the electron population and the ambient corona, such as density, magnetic field strength, and plasma turbulence level. For a detailed discussion of the emission mechanisms, see the chapter Patra et al. (2026) in this book. Table 3 provides a summary of the diagnostics that are possible employing solar radio bursts. We also highlight the complementarity of radio observations with observations across the other wavelength domains. Figure 14 shows a combined plot of the radio observations, AIA EUV images, and white–light coronagraph data. This highlights the complementarity of radio observations with measurements across other wavelength domains. The figure illustrates the temporal and spatial relationship between radio emission and coronal structures observed in EUV. The radio signatures trace energetic electron populations and shock-related processes, while the EUV images reveal the evolving morphology of the coronal plasma. The combined view demonstrates how radio diagnostics provide direct insight into particle acceleration and plasma emission processes that are not accessible through thermal imaging alone. Figure 15 shows the variation of flux density with frequency for different classes of solar radio bursts across the SKA frequency bands. The figure emphasizes how distinct burst types dominate different frequency regimes, reflecting changes in emission mechanism and source height in the solar atmosphere. Coherent plasma emission processes dominate at low frequencies, producing high brightness temperatures, while incoherent gyrosynchrotron emission becomes increasingly important at higher frequencies. This frequency-dependent behavior underscores the importance of broad spectral coverage to fully

Table 3: Summary of the physical diagnostics provided by solar radio burst observations and their complementarity with measurements at other wavelengths.

Observation from Radio Bursts	Physical Information Provided	Complementarity with Other Wavelengths
Plasma Emission (Types I–V)	Electron density, plasma frequency, height of emission, coronal structure; diagnostics of shock speeds (Type II) and electron beam speeds (Type III).	Complements EUV/X-ray by probing regions where EUV is optically thick or faint; reveals dynamics beyond coronagraph field-of-view; provides density diagnostics not accessible in EUV imaging.
Electron Acceleration Signatures	Fast electron beams (Type III), trapped electrons (Type IV), microbursts, turbulence.	Hard X-rays observe thick-target bremsstrahlung from footpoints; radio observations, on the other hand, reveal coronal acceleration and transport, providing a coronal counterpart to HXR sources.
Shock Waves and CME Diagnostics	CME-driven shock speed, Mach number, shock geometry, height–time profile (Type II bursts).	Complements coronagraph CME observations by detecting shocks even when CME fronts are faint; links coronagraph kinematics to shock formation height and SEP production.
Magnetic Field Diagnostics	Gyrosynchrotron emission (GHz), polarization, magnetic field strength and topology, coronal B-field evolution.	Optical/EUV magnetography only measures photospheric fields; radio provides direct measurements of coronal magnetic fields, filling the gap between photospheric (optical) and in-situ measurements.
Thermal and Non-thermal Energy Release	Flare continua, gyrosynchrotron spectra, accelerated electron distributions, energy partition.	Soft X-rays measure thermal plasma; radio provides non-thermal signatures, allowing a complete energy budget of flares when combined with GOES/SXR.
Large-scale Coronal Propagation	Tracing electron beams and shocks through the corona and heliosphere (decametric–kilometric bursts).	Complements in-situ spacecraft (Wind, PSP, Solar Orbiter) by linking remote-sensed radio bursts with in-situ particle and wave measurements along magnetic field lines.
Heliospheric Imaging (Spacecraft)	Low-frequency radio triangulation, direction-finding, and source location of Type II/III bursts in the heliosphere.	No other wavelength can remotely detect electron beams and shocks beyond 20 $R_\odot$; it complements white-light heliospheric imagers by probing invisible shocks and magnetic connectivity.

characterise solar eruptive events.

3.3 Current Observations and Challenges

While many solar observing instruments are present worldwide, there is a dearth of dedicated solar imaging instruments, both at low and high frequencies. There is also a 15-20 UT time gap where neither broadband dynamic spectrometers nor imaging telescopes are available. This gap needs to be filled in order to obtain synoptic monitoring of the Sun. Furthermore, instruments that perform imaging are restricted to Stokes I due to difficulties in polarization calibration, as it depends on the telescope's systematic response, the position of the Sun and calibrators in the sky, and the ionosphere at low metric to decametric range frequencies. With advances in ionospheric monitoring, learned from LOFAR, and in polarization calibration, learnt from MWA, some of these challenges can be resolved in the upcoming decade using the SKA.

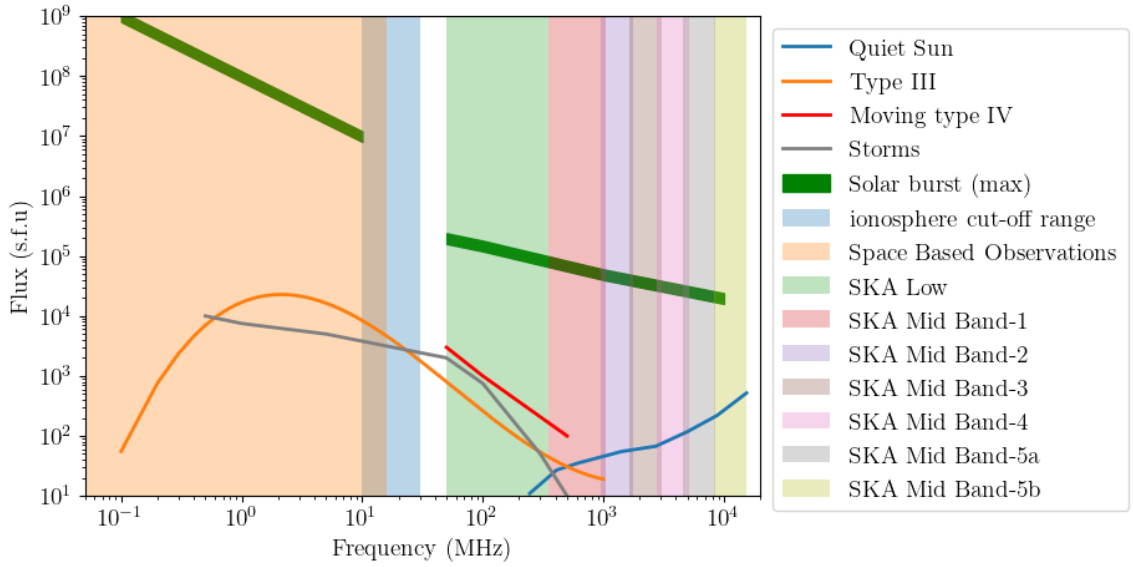

Figure 15: The variation of flux density with frequency for different types of solar radio bursts. This illustrates how burst intensity changes across the observed spectral range.

4 SKA Capabilities for Solar Science

4.1 Solar Radio Monitoring

SKA, with its unprecedented frequency coverage, will enable monitoring solar bursts from the low corona to the inner heliosphere. SKA Low has 256 dual-polarized log-periodic dipoles operating between 50 and 350 MHz. A single station will have a field of view of $\approx 90^o$, enabling solar monitoring of $\sim$ 6 hours. The SEFD of a single SKA station has been measured to be $\approx$ 5.4 kJy at 90 MHz, while it is 3.7 kJy at 310 MHz. Either way, the sensitivity will be at a sub-SFU level, facilitating the detection of weak bursts. Each station can form 48 beams, out of which one Solar beam will allow us to achieve most of the monitoring requirements.

The data from the monitor beam can be searched for events using the native SKA Low time and frequency resolution. Data containing interesting events can be stored for detailed analysis, while an averaged version of the dynamic spectra can be used for long-term archival purposes.

While obtaining a solar dedicated beam may not be possible with SKA-mid, opportunistic observations can be made using triggers from the SKA-Low monitor beam or from other solar telescope networks after the detection of solar flares. This will be particularly useful for probing impulsive flare-related energy releases in the microwave frequency range. Table 4 summarises the key parameters of SKA1-LOW and SKA1-MID that are most relevant for solar radio physics.

4.2 High time and frequency resolution observations

While solar bursts have been classified into five well-known and understood types (refer to Figure 9), there exists a plethora of fine structure bursts whose association with energy releases in the Sun is not very well understood. The fine structures of the type II and type III bursts can be used to

Table 4: Key parameters of SKA1-LOW and SKA1-MID relevant for solar radio physics.

Parameter	**SKA1-LOW**	**SKA1-MID**
Frequency range	50–350 MHz	0.35–15.3 GHz
Primary science	Plasma emission	Gyrosynchrotron, free-free
Antenna elements	131,072 dipoles	197 dishes (15 m)
Stations / Dishes	512 stations	133 (SA) + 64 MeerKAT
Max. baseline	~65 km	~150 km
Angular resolution	~10" @ 100 MHz	~0.5" @ 10 GHz
Time resolution	<1 ms	<1 ms
Spectral channels	$> 10^4$	$> 10^4$
Instantaneous BW	~300 MHz	~5 GHz
Polarization	Full Stokes	Full Stokes
Solar dedicated	No (but capable)	No (but capable)
Key diagnostics	Type II/III, CME shocks	Flares, coronal heating

understand the propagation effects of the electron beams and shocks in the solar corona, if they are well resolved. With SKA's frequency resolution of ≈ 5 kHz and high time resolution $\sim$ few ms, fine structure bursts can be studied in an unprecedent way. For instance, striae in type III bursts were $\sim$ few 10s of kHz, and lasted a few 10s of ms in duration. These bursts can be sampled to high resolution, and various correlation analyses can be performed on them to understand the nature of plasma turbulence. Similarly, fine structure in type II bursts can also be used for remote sensing of the plasma around the shock front, giving rise to the radio emission. The fine structures often superimposed on the type IV continuum, such as fibers, spikes, pulsations, or zebra patterns (Slottje, 1972; Magdalenić et al., 2006) when fully resolved in both temporal and frequency domains, allow an estimate of the plasma characteristics and reveal information on the associated small-scale process.

4.3 Imaging Spectroscopy and Synthesis Imaging Observations

Imaging spectroscopy is a crucial technique that has gained increasing use in recent years, thanks to the availability of excellent wide-band antennas and affordable signal processing hardware. LOFAR has pioneered this by forming multiple tied-array beamlets[9], which has allowed the localization of radio-emission regions across varying heliocentric distances. Imaging observations of the Sun have been performed using both dedicated and generic radio interferometers. The solar disk in optical wavelengths has a diameter of $\approx 32'$; this becomes larger at low frequencies. Dedicated solar radio interferometers used 'T' shaped grating arrays to achieve a 'filled' uv plane. This may not be suitable for wide-band arrays due to the chromaticity of the grating response.

4.4 Solar Long Baseline Interferometer Observations

Solar long-baseline interferometric observations with the Square Kilometre Array (SKA-Low and SKA-Mid) will provide unprecedented capabilities for high-dynamic range, high-fidelity imaging of the solar corona across a wide frequency range (50 MHz to 15 GHz). The availability of baselines extending up to tens of kilometres enables spatial resolutions of a few arcseconds at low radio

[9]Beams at different frequencies are beamlets in LOFAR parlance

frequencies and sub-arcsecond imaging in the microwave range, surpassing all existing solar radio interferometers. In comparison, current instruments such as the MWA, LOFAR, and EOVSA offer important but more limited baselines, resulting in coarser angular resolutions and lower imaging dynamic range. While MWA and LOFAR provide excellent low-frequency coverage and snapshot spectroscopic imaging, and EOVSA excels in broadband microwave imaging spectroscopy for flare diagnostics, the SKA will combine these capabilities within a single instrument, thus enabling comprehensive diagnostics of coronal plasma, magnetic fields and particle acceleration over multiple spatial scales. Consequently, the SKA is expected to establish a new benchmark for long-baseline solar radio interferometry and substantially enhance the global capability for solar physics and space weather research. Figure 16 shows the comparison of the longest baselines for major global radio interferometers relevant to solar radio physics and high–resolution imaging.

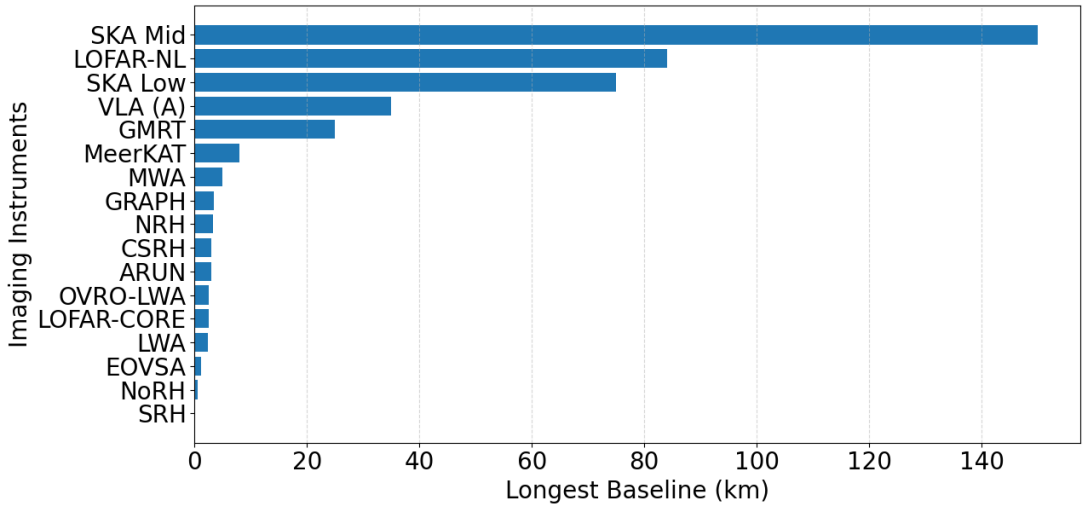

Figure 16: Comparison of the maximum baselines of major radio interferometers used for solar and non-solar radio imaging. Arrays such as LOFAR, VLA, MeerKAT, GMRT and the upcoming SKA provide long-baseline capabilities, enabling high angular resolution essential for studying fine-scale coronal structures and solar radio burst source locations.

4.5 Technical Challenges and Path Forward

SKA has the advantage of a larger frequency bandwidth for solar radio bursts tracking and increased temporal and spectral resolution. Compared to LOFAR, the SKA is also expected to have increased sensitivity over longer baselines, especially with SKA-Low at low frequencies. SKA-Low, combined with SKA-Mid, can also observe Type II and other radio bursts at much higher frequencies compared to LOFAR. High-frequency type II bursts, starting at frequencies above 500 MHz, have been reported on several occasions (e.g., Kumari et al., 2017a; Vasanth et al., 2025), indicating the presence of early low coronal shock waves. The larger observing bandwidth of SKA will enable the tracking of electron beams closer to the erupting region and over longer distances, helping to investigate the formation of coronal shocks. The increased spatial resolution of SKA can determine smaller source sizes or resolve multiple bursts contributing to extended emissions, and in turn be used to deduce properties of the shock (e.g. Morosan et al., 2025b). There is a detailed discussion regarding

the chapter titled 'State-of-the-art Observation, Calibration, and Imaging Framework for Solar and Heliospheric Sciences with SKAO' in this book by Oberoi et al. (2026).

Acknowledgments

A. K., M. V., D. E. M., J. M. and K. D. contributed equally to this work. We acknowledge the CESRA community website curated by Dr. Eduard Kontar for providing valuable resources related to solar radio observations. A. K. acknowledges support from the ANRF Prime Minister's Early Career Research Grant (PM-ECRG) Program. J. M. acknowledges financial support from the BRAIN.be project SWIM, University start-up grant 3E220031, and the FEDtWIN project PERIHELION. K. D. acknowledges the PhD grant from the Royal Observatory of Belgium and the C1 project UnderRadioSun at KU Leuven. We are grateful to the various observatories and instrument teams whose publicly available datasets and documentation enabled the compilation of instrument characteristics and the generation of comparative plots. We also acknowledge the use of the SunPy Python package, along with the broader open-source scientific Python ecosystem.

Appendix

Table 5 presents a summary of the major light–curve instruments used for solar radio observations. Additional details of these instruments are provided in Section 2.1. Table 6 summarises the key solar radio spectrographs and spectropolarimeters currently in operation. Further technical descriptions and references are discussed in Section 2.2. Table 7 provides an overview of the principal radio imaging facilities that contribute to both solar and non-solar science. More detailed information on these telescopes is included in Section 2.3. Together, these tables provide a comprehensive snapshot of the global solar radio observational infrastructure, encompassing time–series monitoring, broadband spectral measurements, and high–resolution imaging. They highlight the diversity of instruments, observing schemes, and frequency coverages that complement each other in studying solar radio bursts and related heliophysical processes.

References

J. K. Alexander et al. The radio astronomy explorer satellite (RAE-1). Technical Report NASA-TM-X-58144, NASA Goddard Space Flight Center, 1970. URL https://ntrs.nasa.gov/citations/19700016708. NASA Technical Memorandum.

J. K. Alexander et al. The radio astronomy explorer satellite RAE-2: Mission, instrumentation, and preliminary results. Technical Report NASA-SP-355, NASA Goddard Space Flight Center, 1975. URL https://ntrs.nasa.gov/citations/19750012988. NASA Special Publication.

C. E. Alissandrakis. *Frontiers in Astronomy and Space Sciences*, Volume 7 - 2020, 2020. ISSN 2296-987X. doi: 10.3389/fspas.2020.574460. URL https://www.frontiersin.org/journals/astronomy-and-space-sciences/articles/10.3389/fspas.2020.574460.

K. Arzner and A. O. Benz. *Solar Physics*, 231(1):117–141, 2005. doi: 10.1007/s11207-005-1590-8. URL https://doi.org/10.1007/s11207-005-1590-8.

S. T. Badman et al. ApJ, 938(2):95, oct 2022. doi: 10.3847/1538-4357/ac90c2. URL https://dx.doi.org/10.3847/1538-4357/ac90c2.

Table 5: Summary of instruments and their operating parameters.

Instrument	Obs. Time (UT)	Channels (GHz)	Data Type
VIRAC RT-32	07–14	[6.3, 9.3]	RCP/LCP
RT-2 / RT-3	05–13	[6.15, 9.35]	Total Intensity
SSRT	07–14	[4.5, 5.2, 6.0, 6.8, 7.5]	Total Intensity
SRH	07–14	[4.5, 5.2, 6.0, 6.8, 7.5]	Total Intensity
SST	17–23	[212, 405]	Total Intensity
SSRT SP	07–14	[2.34, 2.57, 2.85, 3.20, 3.63, 4.16, 4.82, 5.62, 6.60, 7.82, 8.75, 10.10, 13.20, 15.70, 19.90, 22.93]	RCP/LCP
Metsähovi	09–16	[11.2]	Total Intensity
NoRP	22–30	[1, 2, 3.75, 9.4, 17, 35, 80]	RCP/LCP
RSTN	00–24	[0.245, 0.410, 0.610, 1.415, 2.695, 4.995, 8.800, 15.400]	Total Intensity
GRIP	02–08	[0.0795, 0.0805]	Stokes I and V
Ondrejov RT3	07–14	[2.9, 3.1]	Total Intensity

T. S. Bastian, A. O. Benz, and D. E. Gary. ARA&A, 36:131–188, Jan. 1998. doi: 10.1146/annurev.astro.36.1.131.

T. S. Bastian et al. ApJ, 558(1):L65–L69, Sept. 2001. doi: 10.1086/323421.

A. O. Benz. In E. Schanda, editor, *CESRA-4, Committee of European Solar Radio Astronomers*, volume 4, page 157, Jan. 1974.

A. O. Benz et al. *Solar Physics*, 260(2):375–388, Dec 2009. ISSN 1573-093X. doi: 10.1007/s11207-009-9455-1. URL https://doi.org/10.1007/s11207-009-9455-1.

V. Bezrukovs et al. *Latvian Journal of Physics and Technical Sciences*, 49(6):30, 2012.

S. Bhunia, E. P. Carley, D. Oberoi, and P. T. Gallagher. A&A, 670:A169, Feb. 2023. doi: 10.1051/0004-6361/202244456.

S. Bhunia et al. A&A, 695:A136, 2025. doi: 10.1051/0004-6361/202451426. URL https://doi.org/10.1051/0004-6361/202451426.

A. Boischot. *Academie des Sciences Paris Comptes Rendus*, 244:1326–1329, Jan. 1957.

J. L. Bougeret et al. Space Sci. Rev., 71(1-4):231–263, Feb. 1995. doi: 10.1007/BF00751331.

J. L. Bougeret et al. Space Sci. Rev., 136(1-4):487–528, Apr. 2008. doi: 10.1007/s11214-007-9298-8.

I. H. Cairns and R. D. Robinson. Sol. Phys., 111(2):365–383, Sep 1987. doi: 10.1007/BF00148526.

H. V. Cane and S. M. White. Sol. Phys., 120(1):137–144, Mar. 1989. doi: 10.1007/BF00148539.

E. P. Carley et al. *Nature Physics*, 9(12):811–816, Dec. 2013. doi: 10.1038/nphys2767.

B. Cecconi and P. Zarka. *Radio Science*, 40:RS3003, 2005. doi: 10.1029/2004RS003070. URL https://agupubs.onlinelibrary.wiley.com/doi/full/10.1029/2004RS003070.

L. Chen et al. *The Astrophysical Journal Letters*, 975(2):L37, nov 2024. doi: 10.3847/2041-8213/ad89c2. URL https://doi.org/10.3847/2041-8213/ad89c2.

X. Chen et al. ApJ, 990(2):L50, Sept. 2025. doi: 10.3847/2041-8213/adfa71.

G. Cozzani, Y. V. Khotyaintsev, D. B. Graham, and M. André. *Journal of Geophysical Research*

Table 6: Summary of major solar radio spectrographs and their operating parameters.

Instrument	F_l **(MHz)**	F_u **(MHz)**	**Obs. Time (UT)**	**Type**
URAN-2	8	33	07–14	Spectropolarimeter
OSRA	40	800	09–15	Spectrograph
SSRT	4000	8000	07–14[a]	Spectropolarimeter
GLOSS	35	435	02–09	Spectrograph
GRASP	50	500	02–09	Spectropolarimeter
HSRS	275	1495	08.5–16	Spectrograph
HiRAS	25	2500	22–24	Spectrograph
Learmonth	25	180	22–24	Spectrograph
ARTEMIS-IV	20	650	08–15	Spectrograph
IZMIRAN	20	260	07–14	Spectrograph
Ondrejov	800	5000	08–14	Spectrograph
Culgoora	18	1800	22–24	Spectrograph
ETH 5m STS	1415	1432	09–15	Spectrograph
ETH 5m Bleien	1590	1650	09–15	Spectrograph
ETH LWA Bleien	10	80	09–15	Spectropolarimeter
NDA	10	100	09–15	Spectrograph
Phoenix-3	100	5000	09–15	Spectrograph

[a] SSRT has seasonal operation: typically 23–10 UT in summer.

(Space Physics), 128(5):e2022JA031128, May 2023. doi: 10.1029/2022JA031128.

B. Dabrowski et al. *Remote Sensing*, 13(1), 2021. ISSN 2072-4292. doi: 10.3390/rs13010148. URL https://www.mdpi.com/2072-4292/13/1/148.

H. Daene and A. KrüGER. *Astronomische Nachrichten*, 289(3):105–115, Apr. 1966. doi: 10.1002/asna.19662890302.

K. Deshpande et al. *A&A*, 704:A95, 2025. doi: 10.1051/0004-6361/202555142. URL https://doi.org/10.1051/0004-6361/202555142.

P. E. Dewdney, R. Braun, and W. Turner. In *2017 XXXIInd General Assembly and Scientific Symposium of the International Union of Radio Science (URSI GASS)*, pages 1–4. IEEE, 2017.

G. A. Dulk. ARA&A, 23:169–224, Jan. 1985. doi: 10.1146/annurev.aa.23.090185.001125.

G. A. Dulk, D. E. Gary, and S. Suzuki. A&A, 88(1-2):218–229, Aug. 1980.

J. Fainberg and R. G. Stone. *Solar Physics*, 36:401–411, 1974. doi: 10.1007/BF00151688.

N. J. Fox et al. Space Sci. Rev., 204(1-4):7–48, Dec. 2016. doi: 10.1007/s11214-015-0211-6.

D. E. Gary and C. U. Keller, editors. *Solar and Space Weather Radiophysics: Current Status and Future Developments*, volume 314 of *Astrophysics and Space Science Library*. Kluwer Academic Publishers, Dordrecht, 2004. Edited volume, Center for Solar-Terrestrial Research, New Jersey Institute of Technology, Newark, NJ; National Solar Observatory, Tucson, AZ.

D. E. Gary et al. A&A, 152:42–50, Nov. 1985.

D. E. Gary et al. ApJ, 863(1):83, Aug. 2018. doi: 10.3847/1538-4357/aad0ef.

O. Giersch and J. Kennewell. *Radio Science*, 57(8):e2022RS007456, Aug. 2022. doi: 10.1029/2022RS007456.

Table 7: Summary of major radio telescopes used for solar and non-solar radio imaging.

Telescope	F_l (MHz)	F_u (MHz)	Obs. time (U.T.)	Type	Solar Dedicated
GRAPH	40	120	2.5 – 9	Interferometer	Y
CSRH	400	15000	1 – 8	Interferometer	Y
DART	150	450	1 – 8	Interferometer	Y
SunDish	18000	26000	9 – 14	Single Dish	Y
SRH	4000	8000	7 – 14	Interferometer	Y
Metsähovi	37000	37000	9 – 14	Single Dish	Y
NoRH*	17000	34000	22 – 6	Interferometer	Y
EOVSA	1200	18000	14 – 2	Interferometer	Y
OVRO-LWA	10	90	14 – 2	Interferometer	Y
RATAN-600	610	30000	7 – 14	Interferometer	Y
NRH	150	450	8 – 15	Interferometer	Y
ARUN#	1000	12000	2.5 – 9	Interferometer	Y
uGMRT	150	1500	2.5 – 9	Interferometer	N
MWA	80	300	17 – 23	Interferometer	N
LOFAR	10	220	8 – 15	Interferometer	N
MeerKAT	0.58	3500	7 – 14	Interferometer	N
LWA	10	90	20 – 2	Interferometer	N
VLA	1000	50000	20 – 2	Interferometer	N
SKA-Low#	50	350	17 – 23	Interferometer	N
SKA-Mid#	350	15000	7 – 14	Interferometer	N
ALMA	35000	950000	20 – 2	Interferometer	N

F_l and F_u are lower and upper frequencies of operation of the aforementioned instruments.
* NoRH is not operational anymore.
# Upcoming/upcoming-generation radio instruments (ARUN, SKA-Low, SKA-Mid).

M. Gordovskyy et al. ApJ, 925(2):140, Feb. 2022. doi: 10.3847/1538-4357/ac3bb7.

V. V. Grechnev et al. *Solar Physics*, 216(1):239–272, 2003. doi: 10.1023/A:1026153410061. URL https://doi.org/10.1023/A:1026153410061.

Y. Gupta et al. *Current Science*, 113(4):707–714, Aug. 2017. doi: 10.18520/cs/v113/i04/707-714.

P. Henning et al. The first station of the long wavelength array, 2010. URL https://arxiv.org/abs/1009.0666.

P. A. Henning et al. In J. van Leeuwen, editor, *ISKAF2010 Science Meeting*, page 24, Jan. 2010. doi: 10.22323/1.112.0024.

G. D. Holman and M. E. Pesses. ApJ, 267:837–843, Apr. 1983. doi: 10.1086/160918.

INAF. Sundish project: Single-dish solar radio imaging with inaf radiotelescopes. urlhttps://sites.google.com/inaf.it/sundish, 2025. accessed 29 Nov 2025.

T. James and N. Vilmer. A&A, 673:A57, 2023. doi: 10.1051/0004-6361/202245825. URL https://doi.org/10.1051/0004-6361/202245825.

I. C. Jebaraj et al. A&A, 639:A56, July 2020. doi: 10.1051/0004-6361/201937273.

I. C. Jebaraj et al. A&A, 675:A27, July 2023a. doi: 10.1051/0004-6361/202245716.

I. C. Jebaraj et al. A&A, 670:A20, 2023b. doi: 10.1051/0004-6361/202243494. URL https://doi.org/10.1051/0004-6361/202243494.

J. Jonas and M. Team. *MeerKAT science: on the pathway to the SKA*, page 1, 2016.

K. Kai, D. B. Melrose, and S. Suzuki. Storms. In D. J. McLean and N. R. Labrum, editors, *Solar Radiophysics: Studies of Emission from the Sun at Metre Wavelengths*, pages 415–441. 1985.

M. L. Kaiser et al. Space Sci. Rev., 136(1-4):5–16, Apr. 2008. doi: 10.1007/s11214-007-9277-0.

J. Kandekar and A. Kumari. A&A, 697:L9, May 2025. doi: 10.1051/0004-6361/202553735.

S. R. Kane. *Solar Physics*, 27(1):174–181, 1972. doi: 10.1007/BF00151781.

P. Kaufmann et al. In L. M. Stepp and R. Gilmozzi, editors, *Ground-based and Airborne Telescopes II*, volume 7012 of *Society of Photo-Optical Instrumentation Engineers (SPIE) Conference Series*, page 70120L, July 2008. doi: 10.1117/12.788889.

J. A. Kennewell and D. W. Cornelius. *Australian Physics*, 20(11):276–280, Jan. 1983.

A. Kerdraon and J.-M. Delouis. In G. Trottet, editor, *Coronal Physics from Radio and Space Observations*, volume 483 of *Lecture Notes in Physics, Berlin Springer Verlag*, page 192, 1997. doi: 10.1007/BFb0106458.

I. W. Kienreich, M. Temmer, and A. M. Veronig. ApJ, 703(2):L118–L122, Oct. 2009. doi: 10.1088/0004-637X/703/2/L118.

A. Klassen et al. A&A, 385:1078–1088, Apr. 2002. doi: 10.1051/0004-6361:20020205.

K.-L. Klein, C. Salas Matamoros, A. Hamini, and A. Kollhoff. A&A, 690:A382, Oct. 2024. doi: 10.1051/0004-6361/202450456.

S. A. Knock and I. H. Cairns. *Journal of Geophysical Research: Space Physics*, 110(A1), 2005. doi: https://doi.org/10.1029/2004JA010452. URL https://agupubs.onlinelibrary.wiley.com/doi/abs/10.1029/2004JA010452.

E. P. Kontar et al. *Nature Communications*, 8:1515, Nov. 2017. doi: 10.1038/s41467-017-01307-8.

D. V. Korolkov and I. N. Pariiskii. *Sky and Telescope*, 57:324, Apr. 1979.

V. Krupar et al. *Journal of Geophysical Research: Space Physics*, 117(A06):A06101, 2012. doi: 10.1029/2011JA017333.

V. Krupar et al. Sol. Phys., 289, 2014a.

V. Krupar et al. Sol. Phys., 289(8):3121–3135, Aug 2014b. doi: 10.1007/s11207-014-0522-x.

V. Krupar et al. *The Astrophysical Journal*, 826:66, 2016. doi: 10.3847/0004-637X/826/1/66.

V. Krupar et al. ApJ, 985(2):L27, June 2025. doi: 10.3847/2041-8213/add688.

A. Kumari. *Development of cross-polarized log-periodic dipole antenna for low frequency radio spectral observations*. PhD thesis, Indian Institute of Astrophysics, 2015. Masters dissertation.

A. Kumari. *Radio polarimetric imaging of the solar corona at low frequencies*. PhD thesis, Indian Institute of Astrophysics, 2019. Doctoral dissertation.

A. Kumari. Sol. Phys., 297(7):98, July 2022. doi: 10.1007/s11207-022-02032-2.

A. Kumari, R. Ramesh, C. Kathiravan, and N. Gopalswamy. ApJ, 843:10, July 2017a. doi: 10.3847/1538-4357/aa72e7.

A. Kumari, R. Ramesh, C. Kathiravan, and T. J. Wang. *Solar Physics*, 292(11):161, Nov 2017b. doi: 10.1007/s11207-017-1180-6.

A. Kumari, R. Ramesh, C. Kathiravan, and T. J. Wang. *Solar Physics*, 292(12):177, Dec 2017c. doi: 10.1007/s11207-017-1203-3.

A. Kumari et al. *The Astrophysical Journal*, 881(1):24, Aug 2019. doi: 10.3847/1538-4357/ab2adf.

A. Kumari, D. E. Morosan, and E. K. J. Kilpua. ApJ, 906(2):79, Jan. 2021. doi: 10.3847/1538-4357/abc878.

A. Kumari, D. E. Morosan, E. K. J. Kilpua, and F. Daei. A&A, 675:A102, July 2023. doi: 10.1051/0004-6361/202244015.

A. Kumari et al. A&A, 700:A274, Aug. 2025. doi: 10.1051/0004-6361/202450402.

Y. Leblanc, G. A. Dulk, and S. Hoang. Geophys. Res. Lett., 22(23):3429–3432, 1995. doi: https://doi.org/10.1029/95GL01717. URL https://agupubs.onlinelibrary.wiley.com/doi/abs/10.1029/95GL01717.

S. Lesovoi et al. *Solar-Terrestrial Physics*, 3(1):3–18, Apr. 2017. doi: 10.12737/article_58f96ec60fec52.86165286.

H. Liu et al. Sol. Phys., 293(4):58, Apr. 2018. doi: 10.1007/s11207-018-1280-y.

D. M. Long, P. T. Gallagher, R. T. J. McAteer, and D. S. Bloomfield. ApJ, 680(1):L81, June 2008. doi: 10.1086/589742.

J. Magdalenić. *Solar radio emission and diagnostics of solar coronal plasma*. PhD thesis, University of Zagreb, Faculty of Science, 2008. Ph.D. thesis; Advisors: Bojan Vršnak, Henry Aurass.

J. Magdalenić, B. Vršnak, and H. Aurass. In A. Wilson, editor, *Solar Variability: From Core to Outer Frontiers. The 10th European Solar Physics Meeting*, volume 1 of *ESA Special Publication*, pages 335–338, Noordwijk, 2002. ESA Publications Division. ISBN 92-9092-816-6. Bibliographic Code: 2002ESASP.506..335M.

J. Magdalenić, B. Vršnak, and H. Aurass. In A. Wilson, editor, *Solar Variability: From Core to Outer Frontiers*, volume 1 of *ESA Special Publication*, pages 335–338, Dec. 2002.

J. Magdalenić et al. *The Astrophysical Journal*, 642(1):L77–L80, 2006. doi: 10.1086/504521.

J. Magdalenić et al. *Solar Physics*, 253(1):305–317, 2008. ISSN 1573-093X. doi: 10.1007/s11207-008-9220-x. URL https://doi.org/10.1007/s11207-008-9220-x.

J. Magdalenić et al. ApJ, 791(2):115, Aug. 2014. doi: 10.1088/0004-637X/791/2/115.

J. Magdalenić et al. ApJ, 897(1):L15, July 2020. doi: 10.3847/2041-8213/ab9abc.

S. Majumdar et al. Sol. Phys., 296(4):62, Apr. 2021. doi: 10.1007/s11207-021-01810-8.

G. Mann et al. A&AS, 119:489–498, Nov. 1996.

G. Mann et al. *A&A*, 611:A57, 2018. doi: 10.1051/0004-6361/201629017.

D. J. McLean and N. R. Labrum. *Solar Radiophysics: Studies of Emission from the Sun at Metre Wavelengths*. Cambridge University Press, Cambridge, UK, 1985.

G. Meeks, W. and B. Massey, E.˙ *AIAA Papers*, 90(3855):–, 1990.

V. N. Melnik et al. ApJ, 885(1):78, Nov. 2019. doi: 10.3847/1538-4357/ab46aa.

D. B. Melrose. PASA, 2(5):261–263, Sept. 1974. doi: 10.1017/S1323358000013801.

D. B. Melrose. Sol. Phys., 43(1):211–236, July 1975. doi: 10.1007/BF00155154.

D. B. Melrose. Space Sci. Rev., 26(1):3–38, May 1980. doi: 10.1007/BF00212597.

C. Mercier and G. Trottet. ApJ, 474(1):L65–L68, Jan. 1997. doi: 10.1086/310422.

M. Messerotti and P. Zlobec. *Mem. Soc. Astron. Italiana*, 72:633, 2001. TSRS: Trieste Solar Radio System.

Metsähovi Radio Observatory. Metsähovi radio observatory public solar database. https://etsin.fairdata.fi/dataset/173e31f9-744d-4092-8968-b29c5684cadb, 2019. Accessed 29 Nov 2025.

A. Mohan, P. I. McCauley, D. Oberoi, and A. Mastrano. ApJ, 883(1):45, Sept. 2019. doi:

10.3847/1538-4357/ab3a94.
A. Mohan et al. ApJ, 971(1):86, Aug. 2024. doi: 10.3847/1538-4357/ad5315.
S. Mondal et al. *Solar Physics*, 300(8):109, 2025.
D. E. Morosan et al. *Nat. Astron.*, 3:452–461, Feb 2019. doi: 10.1038/s41550-019-0689-z.
D. E. Morosan, E. K. Kilpua, E. P. Carley, and C. Monstein. *Astronomy & Astrophysics*, 623:A63, 2019.
D. E. Morosan, E. K. J. Kilpua, E. P. Carley, and C. Monstein. A&A, 623:A63, Mar 2019. doi: 10.1051/0004-6361/201834510.
D. E. Morosan et al. A&A, 635:A62, Mar. 2020. doi: 10.1051/0004-6361/201937133.
D. E. Morosan, A. Kumari, E. K. J. Kilpua, and A. Hamini. A&A, 647:L12, Mar. 2021. doi: 10.1051/0004-6361/202140392.
D. E. Morosan et al. A&A, 668:A15, Dec. 2022a. doi: 10.1051/0004-6361/202244432.
D. E. Morosan et al. Sol. Phys., 297(4):47, Apr. 2022b. doi: 10.1007/s11207-022-01976-9.
D. E. Morosan et al. Sol. Phys., 297(4):47, Apr. 2022c. doi: 10.1007/s11207-022-01976-9.
D. E. Morosan et al. A&A, 693:A296, Jan. 2025a. doi: 10.1051/0004-6361/202452511.
D. E. Morosan et al. A&A, 695:A70, Mar. 2025b. doi: 10.1051/0004-6361/202452775.
V. Mugundhan et al. ApJ, 831(2):154, Nov. 2016. doi: 10.3847/0004-637X/831/2/154.
V. Mugundhan, K. Hariharan, and R. Ramesh. Sol. Phys., 292(11):155, Nov. 2017. doi: 10.1007/s11207-017-1181-5.
V. Mugundhan et al. *Solar Physics*, 293(3):41, 2018.
V. Mugundhan et al. ApJ, 855:L8, Mar. 2018. doi: 10.3847/2041-8213/aaaf64.
D. Müller et al. A&A, 642:A1, Oct. 2020. doi: 10.1051/0004-6361/202038467.
P. C. Murphy et al. A&A, 645:A11, Jan. 2021. doi: 10.1051/0004-6361/202038518.
S. Musset et al. A&A, 656:A34, 2021. doi: 10.1051/0004-6361/202140998. URL https://doi.org/10.1051/0004-6361/202140998.
H. Nakajima et al. PASJ, 37(1):163–170, Mar. 1985. doi: 10.1093/pasj/37.1.163.
V. M. Nakariakov et al. *arXiv preprint arXiv:1507.00516*, 2015.
G. J. Nelson and D. B. Melrose. In D. J. McLean and N. R. Labrum, editors, *IN: Solar radiophysics: Studies of emission from the sun at metre wavelengths. Cambridge and New York, Cambridge University Press.*, pages 333–359, 1985a.
G. J. Nelson and D. B. Melrose. Type II bursts. In D. J. McLean and N. R. Labrum, editors, *Solar Radiophysics: Studies of Emission from the Sun at Metre Wavelengths*, pages 333–359. 1985b.
G. Newkirk, Jr. ApJ, 133:983, May 1961a. doi: 10.1086/147104.
G. J. Newkirk. ApJ, 133:983, May 1961b. doi: 10.1086/147104.
A. Nindos, E. P. Kontar, and D. Oberoi. *Advances in Space Research*, 63(4):1404–1424, Feb. 2019. doi: 10.1016/j.asr.2018.10.023.
S. Normo et al. A&A, 698:A175, June 2025. doi: 10.1051/0004-6361/202553702.
D. Oberoi et al. In *Advancing Astrophysics with the SKA – II (AASKAII)*. 2026. arXiv search: Report number AASKAII/Oberoi01.
K. W. Ogilvie, L. F. Burlaga, and R. J. Fitzenreiter. *IEEE Trans. Geosci. Electron.*, GE-16(3): 225–230, 1978. doi: 10.1109/TGE.1978.294575.
G. Paesold and A. O. Benz. A&A, 351:741–746, Nov. 1999. doi: 10.48550/arXiv.astro-ph/0001262.
G. Paesold and A. O. Benz. A&A, 401:711–720, Apr. 2003. doi: 10.1051/0004-6361:20030113.

D. Patra et al. In *Advancing Astrophysics with the SKA – II (AASKAII)*. 2026. arXiv search: Report number AASKAII/Patra01.

R. A. Perley, C. J. Chandler, B. J. Butler, and J. M. Wrobel. ApJ, 739(1):L1, Sept. 2011. doi: 10.1088/2041-8205/739/1/L1.

M. Pick. Sol. Phys., 104(1):19–32, Mar. 1986. doi: 10.1007/BF00159942.

H. Porsche. The Helios mission. Technical Report NASA-SP-385, Max-Planck-Institut für Aeronomie / NASA Goddard Space Flight Center, 1977. URL https://ntrs.nasa.gov/citations/19770013694. NASA Special Publication describing the Helios 1 spacecraft and mission objectives.

H. Porsche. The Helios 2 mission: Spacecraft and results. Technical Report NASA-SP-402, Max-Planck-Institut für Aeronomie / NASA Goddard Space Flight Center, 1979. URL https://ntrs.nasa.gov/citations/19790021480. NASA Special Publication summarizing the Helios 2 mission launched 15 January 1976.

R. Ramesh, K. R. Subramanian, M. S. SundaraRajan, and C. V. Sastry. Sol. Phys., 181(2):439–453, Aug. 1998. doi: 10.1023/A:1005075003370.

R. Ramesh, K. Sasikumar Raja, C. Kathiravan, and A. S. Narayanan. ApJ, 762(2):89, Jan. 2013. doi: 10.1088/0004-637X/762/2/89.

H. A. S. Reid and E. P. Kontar. A&A, 577:A124, 2015. doi: 10.1051/0004-6361/201425309. URL https://doi.org/10.1051/0004-6361/201425309.

H. A. S. Reid and E. P. Kontar. A&A, 606:A141, Oct. 2017a. doi: 10.1051/0004-6361/201730701.

H. A. S. Reid and E. P. Kontar. A&A, 606:A141, 2017b. doi: 10.1051/0004-6361/201730701. URL https://doi.org/10.1051/0004-6361/201730701.

H. A. S. Reid and E. P. Kontar. *Nature Astronomy*, 5:796–804, May 2021. doi: 10.1038/s41550-021-01370-8.

H. A. S. Reid and H. Ratcliffe. *Research in Astronomy and Astrophysics*, 14(7):773–804, July 2014. doi: 10.1088/1674-4527/14/7/003.

H. A. S. Reid, N. Vilmer, and E. P. Kontar. A&A, 529:A66, 2011. doi: 10.1051/0004-6361/201016181. URL https://doi.org/10.1051/0004-6361/201016181.

M. J. Reiner, J. Fainberg, M. L. Kaiser, and R. G. Stone. J. Geophys. Res., 103:1923, Feb. 1998. doi: 10.1029/97JA02646.

W. Riedler and O. F. Krüger. The International Sun–Earth Explorer mission (ISEE-1 and ISEE-2): Spacecraft and experiments. Technical Report NASA-SP-385, NASA / European Space Agency, 1977. URL https://ntrs.nasa.gov/citations/19770013694. NASA Special Publication describing spacecraft design and payload of ISEE-1 and ISEE-2.

R. D. Robinson. *ApJ*, 222:696–706, 1978. Bibliographic Code: 1978ApJ...222..696R.

R. D. Robinson. Sol. Phys., 104(1):33–39, Mar. 1986. doi: 10.1007/BF00159943.

P. Saint-Hilaire, N. Vilmer, and A. Kerdraon. ApJ, 762(1):60, dec 2012a. doi: 10.1088/0004-637X/762/1/60. URL https://dx.doi.org/10.1088/0004-637X/762/1/60.

P. Saint-Hilaire, N. Vilmer, and A. Kerdraon. *The Astrophysical Journal*, 762(1):60, 2012b.

K. Saito, A. I. Poland, and R. H. Munro. Sol. Phys., 55(1):121–134, Nov. 1977. doi: 10.1007/BF00150879.

C. Salas-Matamoros and K.-L. Klein. A&A, 639:A102, July 2020. doi: 10.1051/0004-6361/202037989.

I. N. Sharykin, E. P. Kontar, and A. A. Kuznetsov. Sol. Phys., 293(8):115, Aug. 2018. doi: 10.1007/s11207-018-1333-2.

C. Slottje. *Solar Physics*, 25(1):210–231, 1972.

S. F. Smerd. *Proc. Astron. Soc. Aust.*, 1(7):305–308, Apr 1970. doi: 10.1017/S1323358000012030.

S. F. Smerd, K. V. Sheridan, and R. T. Stewart. Astrophys. Lett., 16:23, Feb. 1975.

G. Y. Smolkov et al. Ap&SS, 119(1):1–4, Jan. 1986. doi: 10.1007/BF00648801.

J. L. Steinberg, S. Hoang, and G. A. Dulk. *A&A*, 150(2):205–216, 1985.

R. T. Stewart. Sol. Phys., 58(1):121–126, June 1978. doi: 10.1007/BF00152558.

E. C. Stone et al. Voyager 1 mission description. Technical Report NASA-SP-4208, NASA Jet Propulsion Laboratory, 1977. URL https://ntrs.nasa.gov/citations/19770026070. NASA Special Publication describing the spacecraft, instruments, and mission objectives.

E. C. Stone et al. Voyager 2: Mission description and early results. Technical Report NASA-SP-438, NASA Jet Propulsion Laboratory, 1979. URL https://ntrs.nasa.gov/citations/19790017575. NASA Special Publication describing the Voyager 2 mission and Jupiter encounter results.

S. Suzuki and G. A. Dulk. Bursts of type III and type V. In D. J. McLean and N. R. Labrum, editors, *Solar Radiophysics: Studies of Emission from the Sun at Metre Wavelengths*, pages 289–332. Cambridge University Press, 1985, 1985.

S. J. Tingay et al. PASA, 30:e007, Jan. 2013. doi: 10.1017/pasa.2012.007.

D. Tripathi et al. *Proceedings of the International Astronomical Union*, 18(S372):17–27, 2023. doi: 10.1017/S1743921323001230.

A. C. Umuhire et al. *Advances in Space Research*, 68(8):3464–3477, Oct. 2021. doi: 10.1016/j.asr.2021.06.029.

A. Valentino and J. Magdalenić. A&A, 690:A137, 2024. doi: 10.1051/0004-6361/202449521. URL https://doi.org/10.1051/0004-6361/202449521.

M. P. van Haarlem et al. A&A, 556:A2, Aug. 2013. doi: 10.1051/0004-6361/201220873.

V. Vasanth. *Solar Physics*, 299(5):63, 2024. ISSN 1573-093X. doi: 10.1007/s11207-024-02293-z. URL https://doi.org/10.1007/s11207-024-02293-z.

V. Vasanth et al. ApJ, 870(1):30, Jan. 2019. doi: 10.3847/1538-4357/aaeffd.

V. Vasanth, Y. Chen, and G. Michalek. *arXiv e-prints*, art. arXiv:2505.02991, May 2025. doi: 10.48550/arXiv.2505.02991.

Vocks, C. et al. In *EGU23, the 25th EGU General Assembly*, 2023. doi: 10.5194/egusphere-egu23-12283. URL https://doi.org/10.5194/egusphere-egu23-12283. EGU-12283.

B. Vršnak and S. Lulić. *Solar Physics*, 196(1):157–180, 2000a. ISSN 1573-093X. doi: 10.1023/A:1005236804727. URL https://doi.org/10.1023/A:1005236804727.

B. Vršnak and S. Lulić. *Solar Physics*, 196(1):181–197, 2000b. ISSN 1573-093X. doi: 10.1023/A:1005288310697. URL https://doi.org/10.1023/A:1005288310697.

B. Vršnak et al. Sol. Phys., 214:325–338, June 2003. doi: 10.1023/A:1024273512811.

B. Vršnak, H. Aurass, J. Magdalenić, and N. Gopalswamy. A&A, 377:321–329, Oct 2001. doi: 10.1051/0004-6361:20011067.

B. Vršnak, J. Magdalenić, H. Aurass, and G. Mann. A&A, 396:673–682, Dec 2002. doi: 10.1051/0004-6361:20021413.

A. Warmuth. *Living Reviews in Solar Physics*, 12(1):3, Sept. 2015. doi: 10.1007/lrsp-2015-3.

D. F. Webb and T. A. Howard. *Living Reviews in Solar Physics*, 9(1):3, Dec. 2012. doi: 10.12942/lrsp-2012-3.

L. A. A. Weiss and R. T. Stewart. *Australian Journal of Physics*, 18:143, Apr. 1965. doi: 10.1071/PH650143.

S. M. White et al. In N. Kassim, M. Perez, W. Junor, and P. Henning, editors, *From Clark Lake to the Long Wavelength Array: Bill Erickson's Radio Science*, volume 345 of *ASP Conference Series*, page 176, Dec. 2005.

J. P. Wild. *Australian Journal of Scientific Research A Physical Sciences*, 3:399, Sept. 1950. doi: 10.1071/CH9500399.

J. P. Wild and L. L. McCready. *Aust. J. Sci. Res., Ser. A Phys. Sci.*, 3:387, Sept. 1950.

J. P. Wild, K. V. Sheridan, and A. A. Neylan. *Australian Journal of Physics*, 12:369, Dec. 1959. doi: 10.1071/PH590369.

J. P. Wild, S. F. Smerd, and A. A. Weiss. *Annual Review of Astronomy and Astrophysics*, 1:291, 1963. doi: 10.1146/annurev.aa.01.090163.001451.

R. M. Winglee and G. A. Dulk. ApJ, 310:432, Nov. 1986. doi: 10.1086/164696.

Y. Yan et al. *Frontiers in Astronomy and Space Sciences*, 8:20, Mar. 2021. doi: 10.3389/fspas.2021.584043.

P. Zhang, S. Yu, E. P. Kontar, and C. Wang. ApJ, 885(2):140, Nov. 2019. doi: 10.3847/1538-4357/ab458f.

P. Zhang et al. A&A, 639:A115, July 2020. doi: 10.1051/0004-6361/202037733.

P. Zhang, D. Morosan, A. Kumari, and E. Kilpua. A&A, 683:A123, Mar. 2024a. doi: 10.1051/0004-6361/202347799.

P. Zhang et al. A&A, 684:L22, Apr. 2024b. doi: 10.1051/0004-6361/202449365.

P. J. Zhang, C. B. Wang, and L. Ye. A&A, 618:A165, Oct. 2018. doi: 10.1051/0004-6361/201833260.

V. V. Zheleznyakov and V. V. Zaitsev. Soviet Ast., 12:14, Aug. 1968.

A. N. Zhukov et al. *arXiv e-prints*, (arXiv:2509.00253), 2025. doi: 10.48550/arXiv.2509.00253.

P. Zlobec, M. Messerotti, M. Karlicky, and H. Urbarz. Sol. Phys., 144(2):373–384, Apr. 1993. doi: 10.1007/BF00627601.

P. Zucca et al. A&A, 615:A89, Jul 2018. doi: 10.1051/0004-6361/201732308.

P. Zucca et al. A&A, 703:A271, Nov. 2025. doi: 10.1051/0004-6361/202554348.